

The SRG/eROSITA All-Sky Survey

A comprehensive X-ray analysis of the Hydra I galaxy cluster

Alpish Srivastava^{1,2,*}, Thomas H. Reiprich¹, Angie Veronica¹, Florian Pacaud¹, Jakob Dietl^{1,3}, Fiona Knies⁴, and Manami Sasaki⁴

¹ Argelander-Institut für Astronomie (AIfA), Universität Bonn, Auf dem Hügel 71, 53121 Bonn, Germany

² Dipartimento di Fisica, Università degli studi di Roma ‘Tor Vergata’, Via della Ricerca Scientifica, 1, 00133 Roma, Italy

³ Max-Planck-Institut für Radioastronomie, Auf dem Hügel 69, 53121 Bonn, Germany

⁴ Dr. Karl Remeis Observatory and ECAP, Universität Erlangen-Nürnberg, Sternwartstraße 7, 96049 Bamberg, Germany

Received ... / Accepted ...

ABSTRACT

Context. The Hydra I galaxy cluster (Abell 1060) is a nearby example of a low-temperature cluster that exhibits intermediate cool core (CC) and non-cool core (NCC) properties. Also, little is known about the gas properties and large-scale structure beyond its R_{500} . **Aims.** We aim to extend the characterization of the intracluster medium (ICM) properties at least until R_{200} and study the correlation between the X-ray emission and non-thermal emission within $R = 0.15R_{500}$, and optical/IR galaxy distribution beyond R_{200} . **Methods.** We used data from the first four SRG/eROSITA All-Sky Surveys (eRASS:4) and an archival Chandra observation to image the X-ray emission from Abell 1060. We also used multiwavelength data from TGSS (radio), 2MASS (IR), and NED (optical) to investigate the non-thermal emission, 2D galaxy distribution, and its redshift evolution, respectively. The surface brightness and spectral analyses are also extended until $3R_{200}$ and R_{200} , respectively, following a detailed cosmic X-ray background (CXB) analysis. **Results.** Our fully corrected eROSITA image showcases a relaxed ICM morphology within R_{500} . We detect two weak ICM shocks with Mach number $M \approx 1.5$ near the central galaxy NGC 3311 that coincide with diffuse radio emission along the line of sight. We also model the central surface brightness cusp and the full profile until $3R_{200}$ using a modified β -model. Furthermore, we detect multiple soft X-ray excesses with high spatial correlation with the 2D optical galaxy distribution beyond R_{200} . In particular, the excess in the north has a significance of 5.8σ above the local CXB level. This suggests that Abell 1060’s outskirts are actively accreting baryons. The NED spectroscopic redshift distribution of member galaxies is unimodal with a best-fit mean and standard deviation of 0.0121 ± 0.0027 from a Gaussian fit. We also estimate the average ICM temperature and metallicity of $\langle k_B T \rangle = 2.27^{+0.15}_{-0.11}$ keV and $\langle Z \rangle = 0.19^{+0.05}_{-0.03} Z_\odot$, respectively, from the $0.2-0.5R_{500}$ annulus. Overall, the temperature profile is broadly consistent with the average temperature profiles from hydrodynamical simulation and Suzaku between $0.28R_{200}$ and R_{200} .

Key words. galaxies: clusters: individual: Hydra I – galaxies: clusters: intracluster medium – Cosmology: large-scale structure of Universe – X-rays: galaxies: clusters

1. Introduction

Galaxy clusters are the largest gravitationally bound and virialized objects that originate from the growth and subsequent collapse of initial density perturbations in the early Universe. They serve as large-scale hydrodynamic laboratories that allow us to probe the dynamical state of clusters through X-ray observations of the intracluster medium (ICM). Traditionally, clusters have been classified as either cool core (CC) or non-cool core (NCC) based on the presence of an inward declining ICM temperature structure within $R \sim 0.2R_{200}$ (e.g., Molendi & Pizzolato 2001). Subsequently, Hudson et al. (2010) subclassified CCs into strong cool cores and weak cool cores (WCC) based on their central cooling time, entropy, and the relative position between the X-ray peak and the brightest cluster galaxy. One such WCC candidate is the Hydra I cluster (Abell 1060), which is a member of the Hydra-Centaurus supercluster (e.g., Einasto et al. 2001; Courtois et al. 2013). Due to its proximity (Table 1), it is highly extended in the sky with an $R_{500} = 45'.38$ (Piffaretti et al. 2011). The first observations of the

cluster and its globular cluster distribution were performed in the optical and radio regime (e.g., Kwast 1966; Smith & Weedman 1976; Smyth & Stobie 1980; Richter & Huchtmeier 1983). Specifically, Richter et al. (1982) reported a recession velocity of $v_0 = 3425 \pm 34 \text{ km s}^{-1}$ and a relatively low line of sight velocity dispersion of 676 km s^{-1} .

The inner $R \approx 0.4R_{500}$ of the cluster has been extensively studied in X-rays. Early observations with the EXOSAT and ASCA X-ray telescopes (e.g., Singh et al. 1988; Tamura et al. 1996; Furusho et al. 2001) revealed that the X-ray emission in the core is dominated by the two central galaxies, NGC 3311 and NGC 3309, and the cluster appears to be relaxed. They further reported a total mass (calculated assuming hydrostatic equilibrium) of $M_{\text{tot}} \approx 10^{14} M_\odot$ and flat temperature and metallicity profiles within $R = 20'$, with average values of $k_B T \approx 3.2 \text{ keV}$ and $Z \approx 0.3 Z_\odot$, respectively. Similar results were also obtained by Tamura et al. (2000) using ROSAT PSPC data. In the next decade, several studies utilized Chandra’s superior angular resolution and XMM-Newton’s large effective area to study the X-ray emission from the ICM in detail. Yamasaki et al. (2002) reported that the central galaxies were noted to have

* Corresponding author; asrivastava@astro.uni-bonn.de

small extents ($<20''$) but showed no signs of mutual stripping. They also confirmed that the ICM exhibited a relaxed morphology. Following that, Hayakawa et al. (2004, 2006) observed a peak in the temperature profile of the previously believed isothermal ICM at $R = 2'.25$, followed by a 30% decline in the outskirts. They also reported that the concentration of matter in the central surface brightness cusp is localized within the inner $R = 3'.23$. Moreover, they detected the ram-pressure stripped halo of NGC 3311, which yielded a high metallicity of $Z = 1.5Z_{\odot}$ and an iron mass of $1.9 \times 10^7 M_{\odot}$ within $R \lesssim 5'$. Last but not least, Sato et al. (2007) used two Suzaku pointings to extend their analysis until $R = 27'$ towards the east and observed a similar decline in the temperature profile as Hayakawa et al. (2004, 2006). In the central $R = 5'$, their temperature profile displayed a flat top, which they believed to be an initial phase of a CC. Furthermore, they observed a decline of about 50% in the abundance profiles of heavier elements such as Si, S, and Fe.

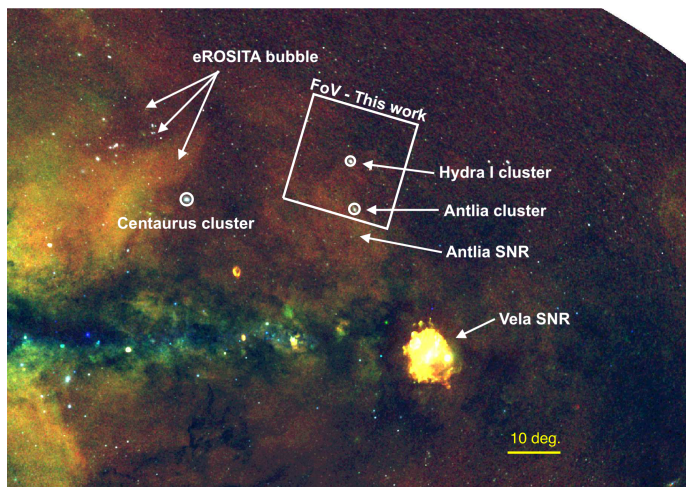


Fig. 1. Zoom-in on half sky eRASS:1 RGB image prepared using broadband TM8 maps in the energy ranges 0.4–0.6 keV (red), 0.6–1.0 keV (green), and 1.0–2.3 keV (blue) from Zheng et al. (2024). The approximate FoV of our eRASS:4 image and other prominent sources in its vicinity are annotated on the image. The circles on the clusters represent their R_{500} .

In radio wavelengths, Lindblad et al. (1985) discovered the radio jets of NGC 3309 via the 6-cm continuum observations from the Very Large Array. However, only a weak radio source was detected in NGC 3311. Recently, Kurahara et al. (2024) discovered diffuse radio emission near NCG 3311 using the Giant Metrewave Radio Telescope (GMRT) data, whose northern section coincides with the stripped halo of NGC 3311 along the line of sight. The rest of the emission extends further to the south-east by approximately $4'$. The source of this emission is unknown, but several plausible scenarios regarding its origin, such as fossil emission from NGC 3311, radio relic, and odd radio circle, are discussed. They also detected radio emission from the spiral galaxy NGC 3312.

Additionally, the Antlia cluster is located about 7° south of Abell 1060 (Fig. 1) and has a similar redshift ($z \approx 0.01$, e.g., Pahre 1999; Wong et al. 2016). The large-scale galaxy distribution suggests that a strand of galaxy filament extends from Antlia to the Centaurus cluster, of which Abell 1060 is in the background (Courtois et al. 2013). Moreover, the highly extended

Antlia supernova remnant (SNR, Zheng et al. 2024, Knies et al., in prep) is also located in projection between the two clusters and dominates the local X-ray foreground there. In Fig. 1, we display the positions of both Abell 1060 and the Antlia cluster relative to the Antlia SNR, the eROSITA bubble (Predehl et al. 2020), and the Galactic plane.

The unexplored ICM as well as the large-scale structure beyond R_{500} , and the presence of a non-thermal component in the core, make Abell 1060 an ideal candidate to study using eROSITA (Predehl et al. 2021) and Chandra (Weisskopf et al. 2000). Recent large field of view (FoV) eROSITA observations of nearby clusters, for example, Virgo (McCall et al. 2024), Fornax (Reiprich et al. 2025), and Centaurus (Veronica et al. 2025) have demonstrated its capability to detect ICM emission from well beyond R_{200} . Furthermore, the softer energy response of eROSITA has been critical in the successful detection and analysis of filamentary X-ray emission between and beyond clusters (e.g., Reiprich et al. 2021; Veronica et al. 2024; Dietl et al. 2024).

In this work, we take advantage of both the aforementioned properties of eROSITA and Chandra’s $1''$ FoV average angular resolution to present an imaging and spectral analysis of Abell 1060 and the surrounding X-ray emission. We focus on the characterization of the surface brightness and gas properties of the ICM at least until R_{200} and perform an indepth analysis of the emission in the inner core. Furthermore, we attempt to correlate the observed X-ray features on all scales with emission in other wavebands in our FoV. Therefore, we structure this paper in the following manner: in Sect. 2, we describe the data reduction process and the subsequent analyses. In Sect. 3, we describe our results and discuss them. Lastly, we summarize our key findings and conclude in Sect. 4.

Table 1. Cluster parameters of Abell 1060 as mentioned in the MCXC catalog (Piffaretti et al. 2011). The central position (J2000) of the cluster is given by the R.A. and Dec., whereas $L_{X,500}$ and M_{500} are the X-ray luminosity in the 0.1–2.4 keV band and the total mass within R_{500} , respectively.

Parameters	Value
z	0.0126
R.A. [$^\circ$]	159.174
Dec. [$^\circ$]	−27.524
$L_{X,500}$ [erg s $^{-1}$]	3.11×10^{43}
M_{500} [M_{\odot}]	9.94×10^{13}
R_{500} [arcmin]	45.38

For our analysis, we used the physical parameters of Abell 1060 from the Meta-Catalog of the compiled properties of X-ray detected Clusters of galaxies (MCXC, Piffaretti et al. 2011) that are mentioned in Table 1. Using the R_{500} from Table 1 and the conversion relations between characteristic radii given in Reiprich et al. (2013), we calculate $R_{2500} = 19'.55$, $R_{200} = 69'.82$, and $3R_{200} = 209'.46$ of Abell 1060. Throughout this work, we assume a flat Λ CDM cosmology with $\Omega_m = 0.3$, $\Omega_\Lambda = 0.7$, and $H_0 = 70 \text{ km s}^{-1} \text{ Mpc}^{-1}$. All error bars are at the 68.3% confidence interval. Moreover, the physical angular scale at the redshift of 0.0126 is $1'' = 0.26 \text{ kpc}$.

2. Data reduction and analysis

2.1. eROSITA data reduction

We used data from the first four SRG/eROSITA All-Sky Surveys (eRASS:1-4) for our analysis. In particular, we utilized 23 sky tiles¹, namely 152117, 153120, 154(114, 123), 155(117, 126), 156120, 157(114, 123), 158(111, 117, 126), 159120, 161(111, 114, 123), 162(117, 126), 163120, 164(114, 123), 165117, and 166120, with Abell 1060 being centered on the tile 158117. The total area of the FoV is roughly $18^\circ \times 18^\circ$ at its maximum extent, and it includes Abell 1060's outskirts ($3R_{200}$ and beyond) and R_{500} of the Antlia cluster (Fig. 1). For the data reduction, we used the eROSITA Science Analysis Software (eSASS, Brunner et al. 2022) version eSASSusers_211214 (eSASS4DR1) with the data processing version c020 and HEASoft² version 6.35. In this work, we adopted the standard naming convention for the eROSITA telescope modules (TMs), i.e., TM1+2+3+4+6 = TM8 (TMs with on-chip filters), TM5+7 = TM9 (TMs without on-chip filters), and TM8+9 = TM0. We also note that, due to the lack of on-chip filters, the low-energy TM9 observations ($\lesssim 0.5$ keV) are severely affected by an optical light leak issue (Predehl et al. 2021) and are therefore removed from our analysis.

We followed the eROSITA data reduction steps as described in Reiprich et al. (2021), Veronica et al. (2024), McCall et al. (2024), Dietl et al. (2024), Veronica et al. (2025), and Reiprich et al. (2025), which we summarize in brief here. We used the eSASS task `evtool` with the arguments `pattern=15` and `flag=0xe00ffff30` to include single, double, triple, and quadruple patterns and to remove bad pixels and the strongly vignetted corners of the CCDs, respectively. In addition, we applied the original good time intervals (GTIs) using the argument `gti="GTI"`. We further extracted the light curves in the hard band 5-10 keV for each sky tile using the task `flaregti` and applied a 3σ threshold to filter out the soft proton flares (SPFs). The GTIs thus acquired are applied to the event lists using `evtool` with the argument `GTI="FLAREGTI"`. For imaging, we primarily used the energy bands 0.2-2.3 keV and 0.5-2.3 keV for TM8 and TM9, respectively. However, despite the differing low energy limits for TM8 and TM9, we label the soft band for TM0 as 0.2-2.3 keV hereafter. We also removed the 1.35-1.6 keV band from the observation because the 1.4 keV Al-K α line was observed to be more prominent in the filter-wheel-closed (FWC) data (Veronica et al. 2025) and could have biased our estimates of the particle induced background (PIB, Freyberg et al. 2020; Yeung et al. 2023).

Furthermore, we created the TM0 PIB map following Eq. 1 from Reiprich et al. (2021). We used the FWC ratio of the soft and hard band (6.7-9.0 keV) counts and the hard band counts from the current observation to estimate the PIB counts in the soft band. We then distributed them throughout our FoV using a normalized flat exposure map (generated using the `expmap` task). Moreover, we also corrected for the variation in the soft X-ray absorption due to the varying total hydrogen column density along the line of sight in our large FoV (Reiprich et al. 2021, Sect. 2.1.4). For this, we used a cut and reprojected HI4PI (HI4PI Collaboration et al. 2016) N_{HI} map and an N_{H_2} map obtained using the Swift³ tool, and combined the two maps following the method described in Willingale et al. (2013) to create the $N_{\text{H,tot}}$ map (Fig. A.1). We report that the median $N_{\text{H,tot}}$

within R_{200} is $5.79 \times 10^{20} \text{ cm}^{-2}$. We then used this $N_{\text{H,tot}}$ map to correct the TM0 exposure map relative to the median $N_{\text{H,tot}}$. Finally, we used the TM0 PIB map and the relative $N_{\text{H,tot}}$ corrected TM0 exposure map to create the fully corrected (background subtracted and exposure corrected) TM0 eROSITA image in the 0.2-2.3 keV band (Fig. B.1).

2.2. Chandra data reduction

We used the Chandra observation (ObsID: 2220) of Abell 1060, which was performed on 4th June 2001 in the VFaint mode (Very Faint Mode). The total exposure time of the observations is roughly 32 ks. For the data reduction, we used the software Chandra Interactive Analysis of Observations (CIAO, Frusciione et al. 2006) version 4.12 and CALDB⁴ version 4.9.3. Abell 1060 is centered on the ACIS-I3 chip in this observation and thus, we only utilized data from this chip, which covers the central $8' \times 8'$ region of the cluster. Furthermore, we used the `chandra_repro` script to ensure the correct calibrations were used to produce the calibrated, bad pixels removed, and initial GTIs applied level 2 event list. We extracted the light curve of the observation using the CIAO task `dmextract` with a time binning of 20 s. We then filtered out the SPF using the task `lc_clean`, which performed a 3σ clipping around the observed mean count rate of $4.86 \text{ counts s}^{-1}$. After filtering, we obtained a flare-free exposure time of 31.49 ks, which suggests a low SPF contamination in the data. The new GTIs are then applied to the event list using the task `dmcopy`.

We then used the `blanksky` and `blanksky_image` scripts to estimate and subtract the background. The `blanksky` script matches the level 2 event list with a custom background file in the blank sky and "stowed" background datasets present in CALDB. The background file is then reprojected to match the observations, and a scale factor is calculated for each chip present in the observation (Hickox & Markevitch 2006). The `blanksky_image` script then uses the reprojected background file and the scale factors to create a scaled background image. We used the parameter `weight_method=particle` to ensure that the scaling method scales the background by the ratio of the observation counts to the counts in the band 9-12 keV. Through this, we obtained a background subtracted image in the 0.5-2.3 keV band. Finally, we used the `fluximage` task to create the fully corrected flux images in the same energy band.

2.3. Imaging analysis

We performed wavelet filtering of the cleaned TM0 image following the implementation described in Pacaud et al. (2006) and Ramos-Ceja et al. (2019), to enhance the faint extended emission and point sources in our image. As we are primarily interested in the emission from the ICM, we used SExtractor (Bertin & Arnouts 1996) to detect and catalog all the point sources, which allowed us to mask them from further analyses. Additionally, we repeated the entire data reduction procedure for three narrow bands, 0.2-0.8 keV, 0.8-1.2 keV, and 1.2-2.3 keV to create a wavelet filtered RGB image (Section B) that allows us to spatially distinguish between the softer and harder energy components of the diffuse X-ray emission. In addition, we used the SciPy (Virtanen et al. 2020) implementation of the Gaussian gradient magnitude (GGM) filter to enhance the faint gradients of different scales in our image. Several previous studies have used this technique to enhance gradients and study the gas

¹ The entire eRASS sky is divided into 4700 sky tiles of size $3^\circ 6' \times 3^\circ 6'$.

² <https://heasarc.gsfc.nasa.gov/docs/software/heasoft/>

³ <https://www.swift.ac.uk/analysis/nhtot/>

⁴ https://heasarc.gsfc.nasa.gov/docs/heasarc/caldb/caldb_intro.html

structure from X-ray images (e.g., Sanders et al. 2016a,b; Walker et al. 2022; McCall et al. 2024; Veronica et al. 2025). In this work, we specifically used the kernels with $\sigma = 8, 16, 32$, and 64 pixels for eROSITA and $\sigma = 10$ pixels for Chandra. We avoided excising point sources from the eROSITA image because eROSITA’s relatively large PSF results in holes that introduce false gradients in the filtered image. Furthermore, we applied the 6-25 pixels unsharp masking to sharpen the small-scale X-ray features in the Chandra image (e.g., Sanders et al. 2016a). All these images are discussed in Sect. 3.1.

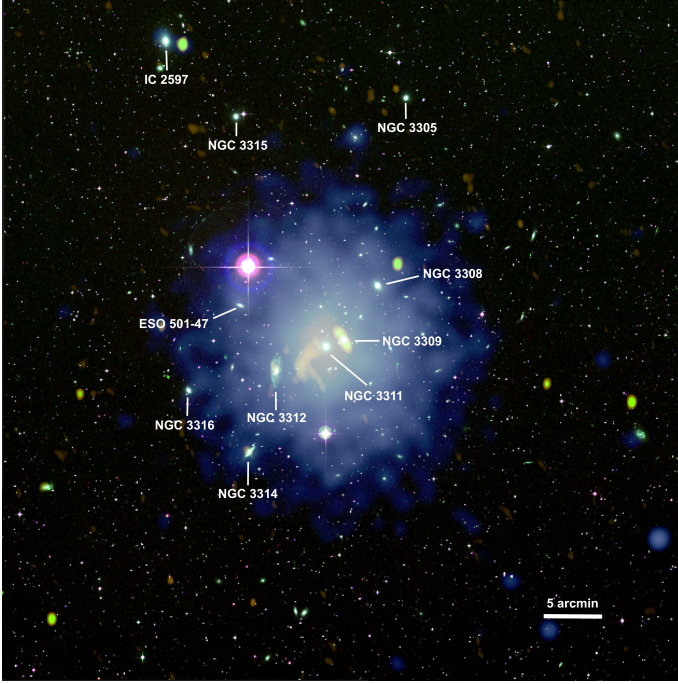


Fig. 2. Combined X-ray (cyan-blue), radio (green), and optical/IR (RGB) overlay of the central region ($\approx 0.8R_{500}$) of Abell 1060. Some of the prominent member galaxies are labeled on the image. The X-ray image is the 0.2-2.3 keV fully corrected TM0 eROSITA image, the radio image is the 150 MHz TGSS image, and the optical image is the DSS2 RGB image (using infrared, red, and blue filters). The A_{\sinh} scaling was applied to the X-ray and radio images to enhance them.

2.4. eROSITA Spectral analysis

We performed an indepth spectral analysis of Abell 1060 to extract the radial distribution of the physical properties of its ICM, for example, gas density, gas temperature, and metal abundance until R_{200} . We used the X-ray spectral fitting software XSPEC (Arnaud 1996) version 12.12.0 and employed C-statistics (Cash 1979) for the fit. Our fitting strategy is based on the eROSITA spectral analyses performed in Ghirardini et al. (2021), Liu et al. (2022), and Veronica et al. (2024, 2025). We used the solar abundance tables from Asplund et al. (2009) and the FWC data of the c020 processing version (Yeung et al. 2023, Appendix A).

For the analysis, we extracted the source and CXB spectra from within R_{200} and eight background regions (Fig. B.1), respectively, from the cleaned TM0 event lists using the eSASS task `srctool`. The output of this task is the spectrum and response files corresponding to each TM from the extraction region. We then rebinned the spectra to have at least one count per

bin using the FT00LS task `grppha`. Furthermore, we modeled the combined emission from the ICM, CXB, and PIB using the following model,

$$\text{Model} = \underbrace{\text{apec}_{\text{LHB}} + \text{TBabs} * (\text{apec}_{\text{MWH}} + \text{nei} + \text{powerlaw})}_{\text{CXB}} + \underbrace{\text{TBabs} * \text{apec}_{\text{ICM}}}_{\text{ICM}} + \text{PIB}. \quad (1)$$

This spectral model consists of three separate components for the CXB, the ICM, and the PIB and is a modified version of the spectral model from Veronica et al. (2024, 2025). Our CXB model consists of thermal `apec` (Smith et al. 2001) components for the local hot bubble (LHB) and the Milky Way halo (MWH), `apecLHB` and `apecMWH`, a constant temperature non-equilibrium ionization model, `nei`⁵, which models the emission from the Antlia SNR (Knies et al., in prep), and a `powerlaw`⁶ component to model the emission from the unresolved active galactic nuclei (AGN). We note that the MWH, SNR, and the unresolved AGN components are affected by the Galactic photoelectric absorption along the line of sight and therefore, a `TBabs` (Wilms et al. 2000) component is multiplied to them. The $N_{\text{H,tot}}$ values used for all the `TBabs` components are extracted from the $N_{\text{H,tot}}$ map in Fig. A.1. Subsequently, we used our CXB model and performed a detailed spectral analysis of the CXB in our FoV, which we describe in Section D. Lastly, we modeled the ICM emission also as an absorbed thermal component, `apecICM`, and the PIB component as a set of power laws, an exponential cut-off, and 23 Gaussian fluorescence lines (more details in Veronica et al. 2025).

We now describe our fitting procedure to estimate the best-fit normalization, temperature, and metallicity of the `apecICM` component. This procedure is similar to the one described in Veronica et al. (2024, 2025) with some minor differences. In our CXB analysis (Section D), we examined the variation in the `apecLHB`, `apecMWH`, and `nei` normalizations between all the background boxes and determined that the box in the north-west (Fig. A.1) is representative of the background within R_{200} . Therefore, we fixed the parameters of the CXB components to the values in Table D.1 and freed their normalizations. We then fitted the CXB spectra from each TM simultaneously with our CXB model by keeping the normalizations linked between them. The energy ranges used for TM8 and TM9 are 0.3-9.0 keV and 0.5-9.0 keV, respectively. Subsequently, we fitted the cluster spectra with the full spectral model (Eq. 1) by setting the obtained best-fit CXB normalizations as the starting point. The `nei` normalization was kept unlinked between the cluster and the CXB fitting, as it varies spatially within R_{200} and showed some degeneracy with the `apecLHB` in our CXB analysis (Section D). Lastly, the redshift of the `apecICM` component was set to $z = 0.0121$ based on our galaxy distribution analysis (Sect. 3.2) and the metallicity was freed along with the normalizations of the PIB component. This is because Veronica et al. (2025) reported a $\approx 0.6\sigma$ variation in the statistical errors when the PIB normalization was frozen. The obtained best-fit values of the ICM normalization, temperature, and metallicity are described in Table E.1.

⁵ <https://heasarc.gsfc.nasa.gov/xanadu/xspec/manual/node200.html>

⁶ <https://heasarc.gsfc.nasa.gov/docs/software/xspec/manual/node221.html>

3. Results and discussion

3.1. X-ray images

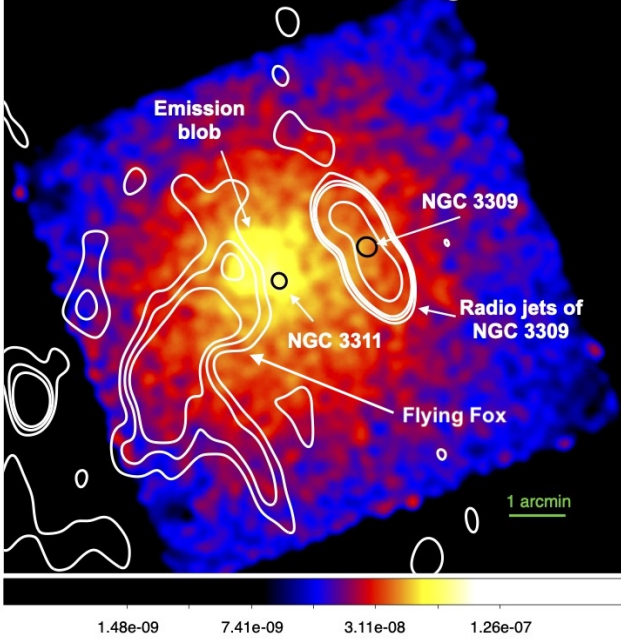


Fig. 3. Fully corrected and point source removed Chandra image in the 0.5-2.3 keV band overlaid with TGSS radio contours. The image is displayed using a logarithmic scale and is smoothed by a Gaussian kernel of $\sigma = 6$ pixels. The black circles mark the excised halos of NGC 3311 and NGC 3309.

We present a multiwavelength view of Abell 1060 within $\approx 0.8R_{500}$ using the X-ray+radio+optical/IR overlay image in Fig. 2. We spatially compared the thermal component of the emission, displayed using the 0.2-2.3 keV eROSITA image and the optical/IR emission, displayed using the Digitized Sky Survey 2 (DSS2, [McLean et al. 2000](#)) infrared, red, and blue images, to establish that the X-ray peak is centered on NGC 3311. The other central galaxy, NGC 3309, is located $\approx 1'.5$ to its west. We also observe the X-ray emission from other prominent members of the cluster, such as the spiral galaxy NGC 3312, NGC 3305, NGC 3308, NGC 3314, NGC 3315, NGC 3316, ESO 501-47, and IC 2597. The overall shape of the X-ray emission from the ICM appears spherically symmetric and showcases an undisturbed morphology with a lack of substructures, which is consistent with the previous studies of the cluster (Sect. 1). We also display the diffuse radio emission from the cluster using the GMRT 150 MHz All-sky Radio Survey, which is a part of the TIFR GMRT Sky Survey (TGSS, [Intema et al. 2017](#)) project in Fig. 2. We note the presence of the diffuse radio source near NGC 3311, which was discovered by [Kurahara et al. \(2024\)](#) and named the Flying Fox (Fig. 3). Other bright radio sources are the radio jets of NGC 3309 and the faint radio emission from NGC 3312. We note that the maximum resolvable scale by the TGSS observations is $68'$, which is comparable to Abell 1060's R_{200} ([Intema et al. 2017](#)). However, we do not detect any cluster-scale diffuse synchrotron emission, for example, radio halos and relics. In the GGM filtered 0.2-2.3 keV eROSITA images (Fig. 4), we only observe small-scale fluctuations in the $\sigma = 8$ and 16 pixels images, and any large-scale shocks or sloshing features with extents of the order of tens or hundreds of kiloparsec are absent. This suggests that Abell 1060 has not undergone any

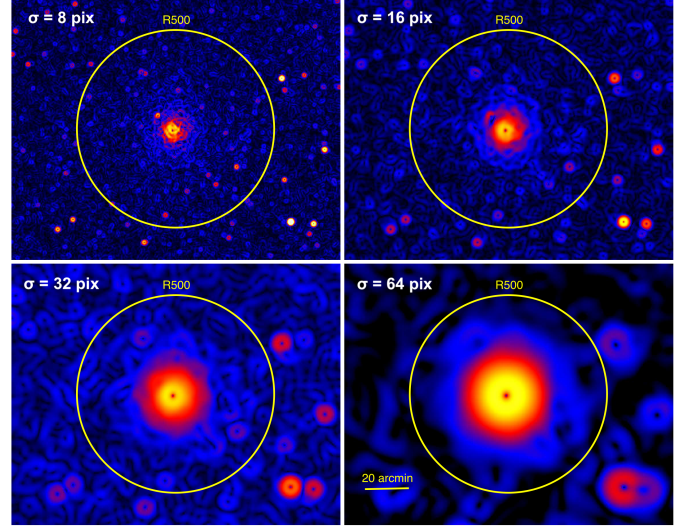


Fig. 4. GGM filtered eROSITA images in the 0.2-2.3 keV band. The kernel size is denoted in the top left corner of each image.

major particle reacceleration event in its recent history, and the majority of the diffuse radio emission is indeed due to galaxy-galaxy and galaxy-ICM interactions within $R < 10'$.

We investigated this intricate interplay between the thermal and non-thermal emission within the inner $8' \times 8'$ region of the cluster using the point source removed 0.5-2.3 keV Chandra image with the TGSS radio contours overlaid on top (Fig. 3). We identify that the stripped halo of NGC 3311 (Sect. 1), labeled as “Emission blob” in the image, has three sharp surface brightness edges towards the south, east, and north. The eastern edge overlaps with the northernmost part of the Flying Fox in projection. We further validated these features using the GGM filtered 0.5-2.3 keV Chandra image (Fig. 5 left), where strong gradients along the southern, eastern, and northern surface brightness edges are visible. These gradients together exhibit a “ Σ ”-shaped structure in the unsharp masked Chandra image (Fig. 5 right). We performed a surface brightness analysis to quantitatively analyze these edges, which is described in Sect. 3.3.2. In addition, contrary to NGC 3311, NGC 3309 shows no signs of extended X-ray emission beyond its excised halo. Also, we do not detect any cavities near its radio jets, which suggests a weak interaction between the jets and the ICM, and its AGN is likely in a quiescent phase. However, this conclusion is limited by the signal-to-noise ratio (S/N) of the current observation (e.g., [Dong et al. 2010](#); [Shin et al. 2016](#)).

We also present the first large-scale view of the X-ray emission from Abell 1060, the Antlia cluster, and the foreground structures in our FoV using the 0.2-2.3 keV eROSITA wavelet filtered image (Fig. 6). We observe a considerable amount of foreground emission beyond Abell 1060's R_{200} that extends predominantly towards the south and west. This emission has high spatial variability, and its various substructures are visibly distinguishable. Therefore, we visually separated these structures, including the emission from the Antlia SNR, into five distinct regions and labeled them from A to E (Fig. 6). Out of these regions, region B contains the majority of the emission from the Antlia SNR (Knies et al., in prep), which obscures the Antlia cluster. Therefore, it is extremely difficult to visually distinguish any extended filamentary emission between the two clusters that might be in the background. We further observe that

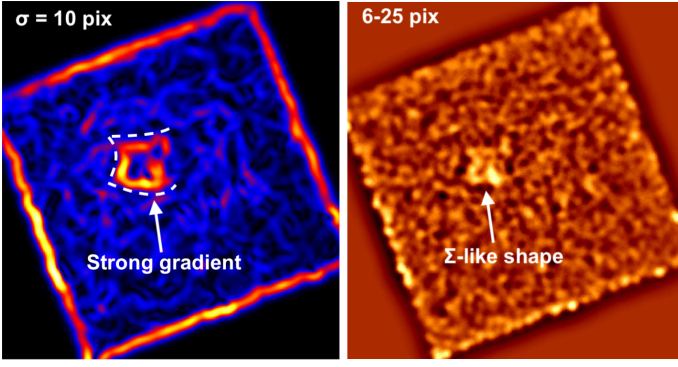


Fig. 5. GGM filtered (left) and unsharp masked (right) Chandra images in the 0.5–2.3 keV band. The kernel sizes and combinations are denoted in the top left corner of each image.

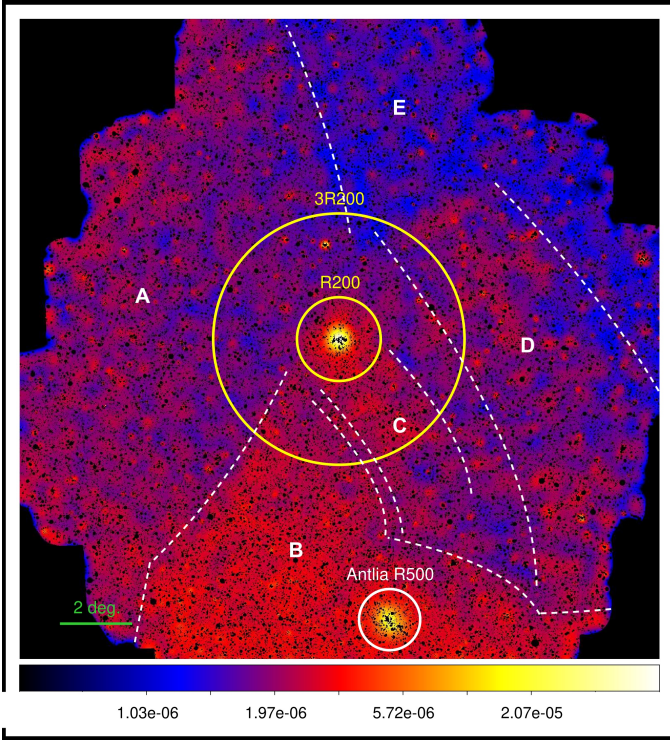


Fig. 6. Point source removed eRASS:4 TM0 wavelet filtered image in the 0.2–2.3 keV band. The image is plotted using a logarithmic scale and has the units counts s^{-1} . The characteristic radii of Abell 1060 (from Table 1) and Antlia (from Wong et al. 2016) are overlaid on the image. Moreover, the distinct foreground structures in the FoV are labeled from A to E.

regions A and D showcase noticeably lower emission as compared to region B, but are highly extended beyond Abell 1060’s $3R_{200}$. On the contrary, the majority of the emission in region C is localized between R_{200} and $3R_{200}$. Lastly, region E, which is located at the northernmost edge of our FoV, showcases a visible lack of foreground structures. From Fig. 1, we further note that the eROSITA bubble is $>10^\circ$ to the east of our FoV and thus, too distant to cause any significant effect on the X-ray foreground. We also notice that the foreground structures in regions A, B, and D extend further beyond our FoV to the south and west, and are prominent in the 0.4–1.0 keV range due to their reddish-green hue. Hence, we can distinguish between the various foreground structures as a function of energy using our

eROSITA RGB image in Fig. B.2. We note that the emission in region B has predominantly a soft spectrum because of its reddish-green color, with the 0.8–1.2 keV component increasing as we move towards the Antlia cluster. Other foreground features throughout the FoV also exhibit a similar composition with varying contributions of 0.2–0.8 keV and 0.8–1.2 keV components. The harder 1.2–2.3 keV component is limited only to the emission from the two clusters and other extended background sources.

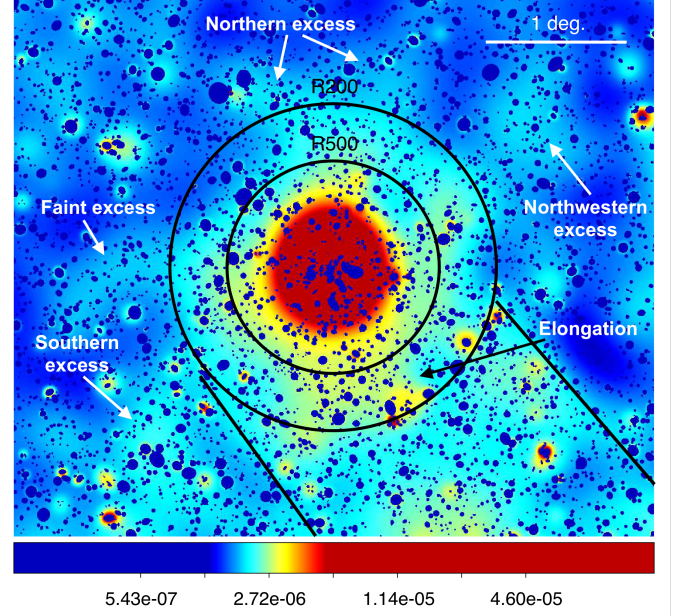


Fig. 7. Same as Fig. 6 but displayed using a different color map and zoomed in on Abell 1060. Prominent X-ray features are labeled on the image, including the foreground emission (between solid black lines) from region C.

In Fig. 7, we showcase the enhanced soft X-ray emission that extends beyond the R_{200} of Abell 1060. Towards the north, we see a bidirectional, low surface brightness excess that further bifurcates towards the north-east and north-west. Similar excesses are also present in the north-west and east. Additionally, we observe a relatively brighter southern excess that is located towards the northernmost corner of region B. However, we suspect that this excess is highly contaminated by the foreground emission from the Antlia SNR. Furthermore, we notice a surface brightness excess between R_{500} and R_{200} in the south that is possibly in part connected to the foreground structure in region C (Fig. 7). We further validate the presence of these excesses via our sector surface brightness analysis in Sect. 3.3.1.

3.2. Galaxy distribution

We performed an optical galaxy redshift analysis of Abell 1060 using the NASA/IPAC Extragalactic Database (NED)⁷ galaxy catalog with a redshift upper limit of $z = 0.1$ and an extent that matches our eROSITA FoV. The redshifts in this catalog are corrected to the Cosmic Microwave Background rest frame, and the breakdown of redshifts in this catalog between spectroscopic, photometric, and redshifts from unknown sources is

⁷ <https://ned.ipac.caltech.edu/byparams>

72.74%, 6.66%, and 20.44%, respectively. For the cluster redshift estimation, we only included galaxies with spectroscopic

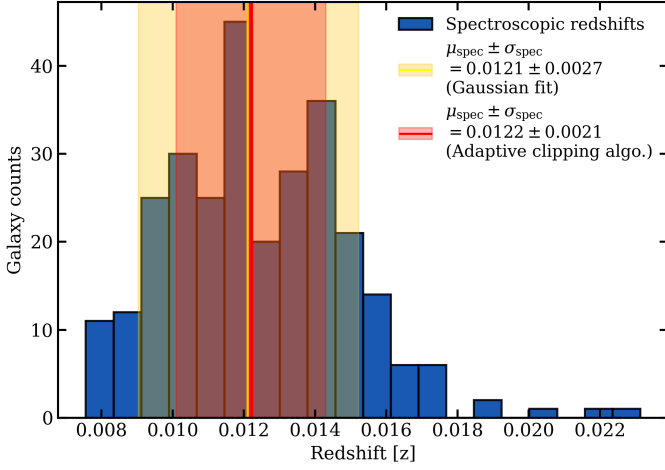


Fig. 8. NED spectroscopic redshift distribution within R_{200} . The obtained mean and standard deviation of the distribution are represented by the solid lines and shaded regions, respectively.

redshifts within R_{200} and $\approx 5\sigma$ range from the MCXC redshift of $z = 0.0126$ (corresponding redshift range $0 \leq z \leq 0.03$), given Abell 1060's line of sight galaxy velocity dispersion of $\sigma_v \approx 700 \text{ km s}^{-1}$ (e.g., [Misingeld et al. 2011](#)). In Fig. 8, we fitted a Gaussian function to this unimodal spectroscopic redshift distribution and obtained a best-fit mean (μ_{spec}) and standard deviation (σ_{spec}) of 0.0121 and 0.0027, respectively. We also applied an adaptive $n\sigma$ -clipping algorithm to this distribution, which yielded a nearly identical redshift estimate of $\mu_{\text{spec}} \pm \sigma_{\text{spec}} = 0.0122 \pm 0.0021$. In both cases, the obtained σ_{spec} is broadly consistent with the literature velocity dispersion of Abell 1060. Moreover, the apparent unimodality in Abell 1060's redshift distribution is in line with the lack of substructure observed in the 0.2-2.3 keV eROSITA image (Fig. 7) within R_{500} . We further investigated the correlation between the X-ray emission and the 2D galaxy distribution in our FoV using the 2MASS galaxy density contours ([Jarrett et al. 2000](#); [Reiprich et al. 2003](#)) and the NED catalog. In Fig. 9, the galaxy distribution within R_{500} shows high spatial correlation with the centrally peaked X-ray emission from the ICM, which is typical for a relaxed cluster. Furthermore, we identified two arm-like galaxy overdensities in Fig. B.3 that extend beyond R_{200} in the west and south-east. The south-eastern overdensity further extends by $\approx 5^\circ$ to the south beyond $3R_{200}$ and overlaps with the foreground structure in region B. However, both these structures consist mainly of background eRASS:1 clusters (e.g., [Bulbul et al. 2024](#)) and galaxies in the redshift range $0.05 \leq z \leq 0.08$, which are unrelated to Abell 1060's galaxy distribution. Nevertheless, several small-scale overdensities closer to R_{200} in the north, north-west, south-west, and south-east are visible in Fig. 9, which implies that at least a fraction of the emission from the southern extended excesses in Fig. 7 belongs to the cluster.

Furthermore, we find no evidence of a galaxy overdensity directly connecting Abell 1060 and the Antlia cluster within the redshift range $0 \leq z \leq 0.03$. However, several indirect overdensities that extend beyond Abell 1060's R_{200} and eventually connect to Antlia's galaxy distribution are apparent in Fig. B.3, which are in the redshift range $0.03 \leq z \leq 0.08$ in the NED catalog. Despite this, the validation of these features using our X-ray images

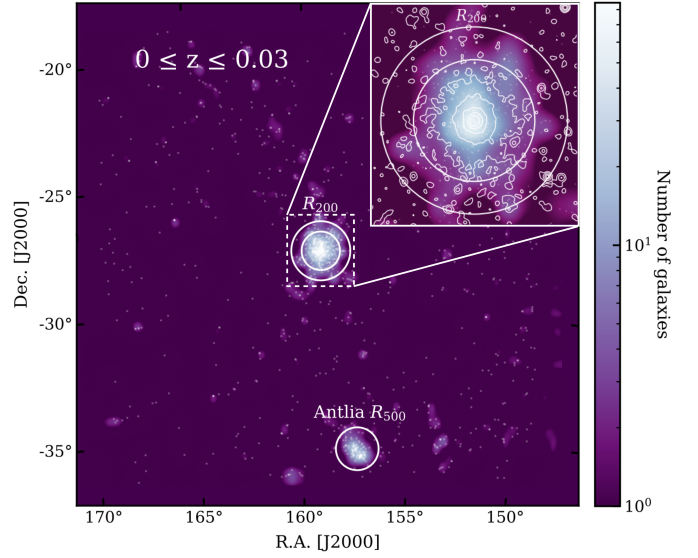


Fig. 9. Galaxy distribution from the NED galaxy catalog reprojected to match our eROSITA FoV, within the redshift range $0 \leq z \leq 0.03$. The inset in the top-right corner is the same image zoomed in on Abell 1060's R_{200} and overlaid with the eROSITA 0.2-2.3 keV X-ray contours. The circle inside R_{200} represents the R_{500} .

is challenging since the relatively high emission measure (EM) foreground emission from the Antlia SNR has a similar temperature (0.15-0.18 keV, [Knies et al., in prep](#)) as compared to the possible filamentary X-ray emission from the warm-hot intergalactic medium (WHIM, ~ 0.01 -0.9 keV, e.g., [Cen & Ostriker 1999](#); [Dietl et al. 2024](#)) that we intend to detect.

3.3. X-ray surface brightness analysis

We extracted the eROSITA surface brightness profile of Abell 1060 until $3R_{200}$ in the 0.2-2.3 keV band, following the procedure described in [Veronica et al. \(2025\)](#) (technical details in Section C). We used eight background boxes of dimensions $3^\circ \times 1^\circ$, each located at $R = 4.5R_{200}$ (Fig. B.1) to estimate the average CXB that is representative of the local X-ray background of Abell 1060. We account for both the statistical uncertainty from each box and the dispersion due to the spatial variation of the foreground between all the boxes by taking the mean and standard deviation of the individual surface brightness values as the average CXB and its uncertainty, respectively. Using this approach, we estimated an average CXB level of $(4.25 \pm 0.63) \times 10^{-4} \text{ counts s}^{-1} \text{ arcmin}^{-2}$. In Fig. 10, we display the CXB subtracted eROSITA profile in the 0.2-2.3 keV band. We also point out that the error bars beyond R_{200} are dramatically enlarged due to poor statistics and the surface brightness being nearly identical to the CXB level.

To model the radial surface brightness distribution of the ICM, we fitted the profile with a modified version of the single β -model (e.g., [Cavaliere & Fusco-Femiano 1976](#)) and the AB-model (e.g., [Pratt & Arnaud 2002](#)) that has the functional form

$$S_X(R) = S_X(0) \left(\frac{R}{r_c} \right)^{-\alpha} \left[1 + \left(\frac{R}{r_c} \right)^2 \right]^{-3\beta + \frac{\alpha}{2} + \frac{1}{2}}, \quad (2)$$

where $S_X(0)$ is the normalization, R is the projected radius, r_c is the core radius, α is the slope of the central power law component, and β is the slope of the overall profile. We used the emcee

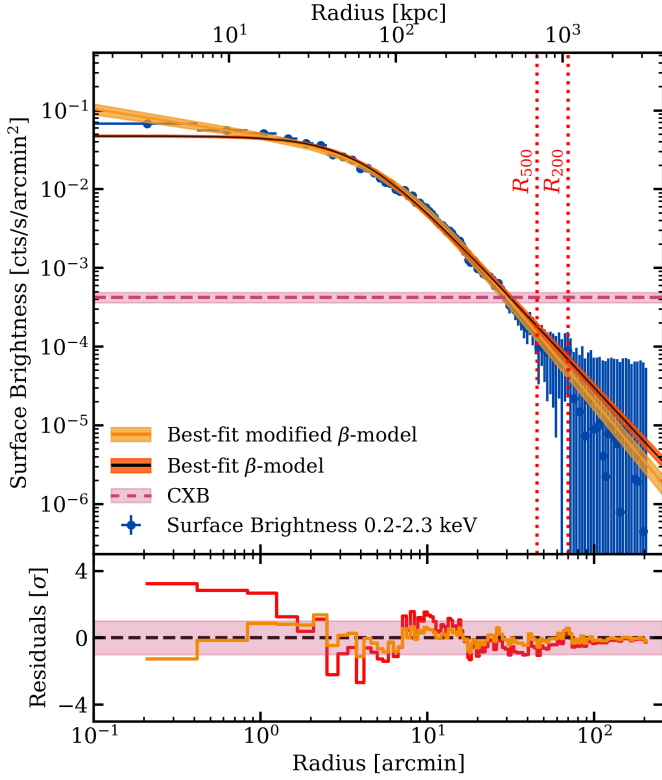


Fig. 10. CXB subtracted eROSITA surface brightness profile of Abell 1060 in the 0.2-2.3 keV band. Also plotted are the best-fit models (orange and red) and average CXB level (pink) with their respective 1σ uncertainties (shaded regions). In the residual plot, the region where the residuals are less than 1σ is shaded in pink.

Markov chain Monte Carlo sampler (Foreman-Mackey et al. 2013) to estimate the posterior distributions of the model parameters, assuming flat priors and a Gaussian likelihood function. The best-fit single and modified β -models are displayed in Fig. 10 and their model parameters are described in Table 2. In the inner three bins, we observe residuals of magnitude $\approx 3.5\sigma$ from the single β -model created by the weak cusp in the profile (Sect. 1). Given the evidence for a relaxed ICM morphology in Sect. 3.1, the presence of this central cusp is expected. Previously, this excess was modeled using an NFW profile (e.g., Tamura et al. 2000) and a double β -model (e.g., Yamasaki et al. 2002; Furusho et al. 2002; Sato et al. 2007). However, the extent of the profiles in these studies was limited to R_{500} and could not capture the entire surface brightness distribution. In our case, we modeled the full extent of the surface brightness distribution until $3R_{200}$ and determined that both these models failed to fit it. On the other hand, Eq. 2 proves to be a good fit ($\chi^2_{\text{red}} = 0.9$) and successfully models the cusp (mean residual of -0.67σ within $R = 1'$) with a power law of slope of $\alpha = 0.33 \pm 0.03$. Interestingly, weak surface brightness cusps with $\alpha < 0.5$ are a typical characteristic of NCC clusters (e.g., Vikhlinin et al. 2007).

Furthermore, Hayakawa et al. (2004) previously estimated best-fit values of $\beta = 0.56^{+0.07}_{-0.05}$ and $r_c = 5.5^{+1.4}_{-1.3}$ using a core excised Chandra profile ($4' \leq R \leq 18'$), which agrees with our β and r_c estimates within error bars. Tamura et al. (2000) and Chen et al. (2007) used ROSAT surface brightness profiles that extended until $1.1R_{500}$ but reported slightly different β and r_c values. Tamura et al. (2000) slightly underestimated the parameter values, while Chen et al. (2007) estimated $\beta = 0.61^{+0.04}_{-0.03}$

Table 2. The best-fit single and modified β -model parameters, χ^2_{red} , and the average CXB level for the 0.2-2.3 keV band.

Parameters	Single β -model	Modified β -model
$S_X(0)^*$	$(2.71 \pm 0.20) \times 10^{-2}$	$(4.74 \pm 0.12) \times 10^{-2}$
r_c [arcmin]	3.97 ± 0.12	5.91 ± 0.33
α	-	0.33 ± 0.03
β	0.55 ± 0.01	0.59 ± 0.01
χ^2_{red}	1.58	0.90
CXB*	$(4.25 \pm 0.63) \times 10^{-4}$	

* units are counts $\text{s}^{-1} \text{arcmin}^{-2}$

and $r_c = 6.08^{+0.97}_{-0.78}$, which is consistent with our estimates within error bars. Additionally, Burns et al. (2008) used N-body and hydrodynamical simulations to obtain a similar β value of ≈ 0.66 for both CC and NCC clusters and r_c values of $(0.05 \pm 0.09)R_{200}$ and $(0.12 \pm 0.02)R_{200}$, respectively. Thus, Abell 1060 again appears to be closer to an NCC cluster on the basis of our r_c value. We also notice a small kink immediately beyond R_{200} in the profile, whose investigation along with the outskirts of Abell 1060 is described in Sect. 3.3.1.

3.3.1. Sector profiles and outskirts

We investigate the directional surface brightness features by splitting the full annulus eROSITA profile into eight sectors, each having an opening angle of $\Delta\varphi = 45^\circ$. We used a similar binning setup as the full annulus profile, but reduced the number of bins between R_{500} and $3R_{200}$ to 35 to improve the S/N. In Fig. C.1, we present the sector surface brightness profiles and the CXB level for each sector, which are plotted together with the full annulus profile. In these sector profiles, we observe some inhomogeneities in the inner core ($R \leq 2'$) and only minor statistical fluctuations in some bins between $0.22R_{500} \leq R \leq R_{500}$ (more details in Section C). Overall, the projected ICM emission from Abell 1060 is highly uniform on large scales up to R_{500} . On the other hand, the outskirts of Abell 1060 are notably complex as most sectors exhibit strong relative variations in surface brightness starting from R_{500} .

In Fig. 11, we display the surface brightness significance (in the unit of σ) above the CXB level, estimated using Eq. C.2, for all the sectors beyond R_{500} . The kink observed in the full annulus profile is only apparent in the southern sector in Figs. C.1 and 11, which originates from the southern elongation (Fig. 7) transitioning into the foreground emission from the Antlia SNR and region C. We also confirm the presence of two soft X-ray excesses in the north and north-west that extend beyond R_{200} (Fig. 7), each of which is detected at a peak significance of 5.8σ and 3.6σ , respectively. Both these excesses showed a particularly high correlation with the 2D galaxy distribution (Sect. 3.2). Furthermore, the northern excess shows a high median surface brightness significance of 3.4σ between R_{200} and $3R_{200}$ in Fig. 11. This is the farthest any significant ICM emission has been detected from Abell 1060. Similar detections in the outskirts of the Centaurus and Fornax clusters have been made using eROSITA (e.g., Veronica et al. 2025; Reiprich et al. 2025). Using this result, we confirm the identification of a virialized northern overdensity using a projected phase-space diagram by Spavone et al. (2024) within $R \approx 1.5R_{200}$ and extend it to $3R_{200}$. This also demonstrates that the north is one of the preferred directions of active accretion in projection. Furthermore, the median significance

value in the south-west between R_{200} and $3R_{200}$ is 4.8σ , but a clear distinction between the ICM and the extended foreground structure in region C is difficult to make despite the presence of a galaxy overdensity beyond R_{200} in this direction. Nevertheless, these signatures suggest that Abell 1060 is actively accreting baryons along multiple directions, and its outskirts are currently being assembled. More et al. (2015) showed that the inner regions of a cluster usually virialize before the outskirts cease to accrete, which is consistent with our identification of multiple X-ray excesses beyond R_{200} , a relaxed ICM (Sect. 3.1), and the weak central cusp (Sect. 3.3) in Abell 1060. In contrast, the

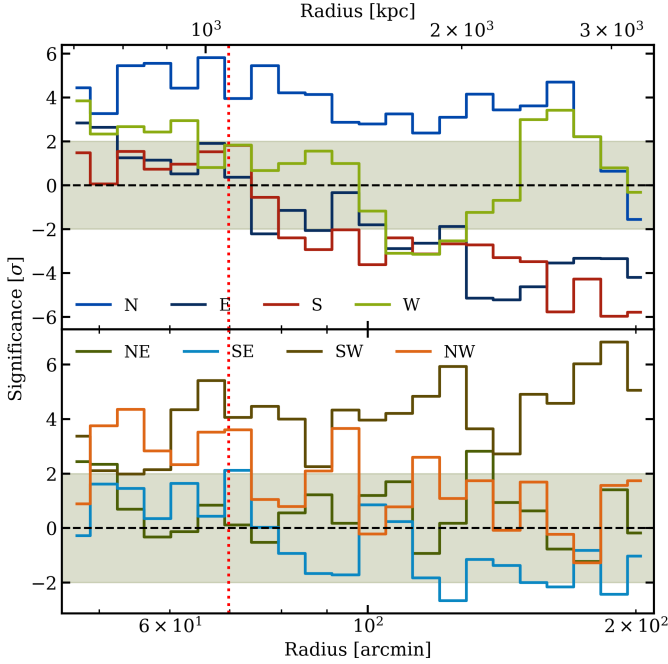


Fig. 11. Surface brightness significance profiles of all eight sectors in the 0.2-2.3 keV band. The shaded region represents significance $\in [-2\sigma, 2\sigma]$ and the dotted vertical line represents the R_{200} .

eastern and southern sectors show negative median significance of 2.6σ and 2.9σ , respectively, beyond R_{200} because the CXB increases radially away from the cluster due to the Antlia SNR and the foreground emission in region A. Meanwhile, the sectors in the south-east and north-east remain within 2σ of the CXB level until $3R_{200}$. The profile in the west declines as expected until $R = 120'$ followed by a sudden rise in surface brightness of significance 3.4σ because of the foreground structure close to $3R_{200}$ in region D (Fig. 6).

3.3.2. Surface brightness discontinuities

We present the surface brightness analysis of the edges of the ram-pressure stripped halo of NGC 3311 (Fig. 5), which we performed using the `pyproffit` (Eckert et al. 2020) package and the 0.5-2.3 keV Chandra image. We extracted the surface brightness profiles within $R = 2'$ from the eastern, southern, and northern directions with an opening angle of $\Delta\varphi = 70^\circ$, based on the visual prominence of the gradients in these directions in Fig. 5. Furthermore, we iteratively adjusted the position and binning of the annuli to ensure that their center is at the X-ray peak orthogonal to the front, and the front is properly sampled in the profile. We then deprojected the surface brightness profiles to extract the

magnitudes of the density jumps across the fronts and their corresponding Mach numbers (M) by fitting them with a broken power law model (e.g., Sarkar et al. 2023) of the form

$$S_X(R) = S_X(0) \int F(\omega)^2 d\omega, \quad (3)$$

where $\omega^2 = R^2 + l^2$, and

$$F(\omega) = \begin{cases} \omega^{-\alpha_1}, & \omega < r_f \\ \frac{1}{J} \omega^{-\alpha_2}, & \omega \geq r_f \end{cases},$$

where $F(\omega)$ is the deprojected density profile, ω is the 3D radius, l is the distance along the line of sight, α_1 and α_2 are the power law indices, J is the ratio of gas density after and before the discontinuity, i.e., ρ_2/ρ_1 , and r_f is the front radius. We further used the expression for a density jump in a polytropic gas that is described as

$$J = \frac{\rho_2}{\rho_1} = \frac{(\gamma + 1)M^2}{(\gamma - 1)M^2 + 2}, \quad (4)$$

where γ is the specific heat ratio, which is equal to $5/3$ for a monoatomic ideal gas (Landau & Lifshitz 1987). Rearranging Eq. 4 to solve for M , we obtain the expression

$$M = \left[\frac{2J}{(\gamma + 1) - J(\gamma - 1)} \right]^{\frac{1}{2}}. \quad (5)$$

For the fit, we used broad, flat priors that allow for a proper exploration of the parameter space without making any assumption about the true value of the parameters. The best-fit parameters and the M values estimated using Eq. 5 for the three sectors are given in Table C.1. In Fig. 12, we display the Chandra surface brightness profiles of the eastern, southern, and northern sectors and their respective best-fit broken power law models. The front is best sampled in the eastern sector, followed by the northern and southern sectors, but the discontinuity is apparent in all of them. Regarding the overall shape of the profiles, we observe small variations in the first four bins, followed by an overall increase in surface brightness at the front ($R \approx 1'$) in both the eastern and southern sectors. This is modeled by the negative α_1 for both these sectors (Table C.1). In contrast, the northern sector has a flatter profile until $R = 1'$, after which a sharp drop of magnitude 3.6σ is seen. However, the magnitude of the best-fit density jump is ≈ 1 , which stayed constant with different robustness tests, for example, varying the bin width and improving the S/N. We also note that beyond the front, the profile transitions from a shallow decline till $R \approx 1.5'$ into a steeper power law-like behavior. A similar profile shape is also observed beyond the front in the east. Furthermore, we note that the density jump at the southern front is the strongest, albeit with the lowest S/N and relatively larger uncertainties on α_1 , J , and M . In addition, the profile in this sector exhibits the flattest slope of $\alpha_2 = 0.64^{+0.03}_{-0.03}$ among all the sectors beyond the front.

We report our estimates of M for both the southern and eastern fronts to be $1.53^{+0.23}_{-0.23}$ and $1.25^{+0.09}_{-0.08}$, respectively, which are weak ICM shocks (e.g., Markevitch & Vikhlinin 2007). In the north, the surface brightness discontinuity corresponds to a marginally subsonic feature with $M = 0.99^{+0.07}_{-0.06}$, although no shock is expected in the ICM for $M < 1$. Kurahara et al. (2024) discussed the possibility of these edges being a sloshing feature, but in our GGM filtered and unsharp masked Chandra images (Fig. 5), this feature is primarily localized near NGC 3311 and lacks any signs of large-scale spiraling gas flows in its vicinity

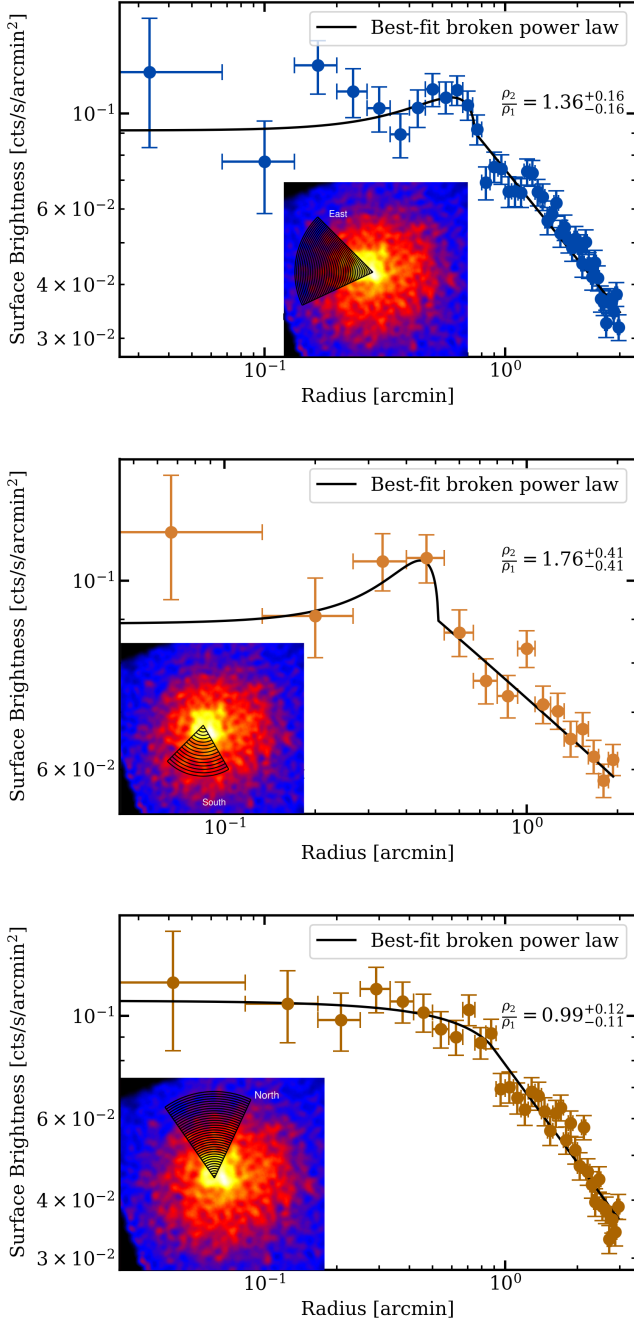


Fig. 12. Chandra surface brightness profiles and the corresponding best-fit broken power law model of three sectors along the east (top), south (middle), and north (bottom) directions in the 0.5–2.3 keV band. The radial extent of these profiles is $R = 2'$. The best-fit value of the parameter J of Eq. 3 is displayed on each plot, and the inset displays the orientation of the sectors using the 0.5–2.3 keV Chandra image.

and closer to NGC 3309. Furthermore, other examples of ongoing ram-pressure stripping in galaxy groups, such as NGC 1404 in the Fornax cluster (Machacek et al. 2005) and NGC 4452 in the Virgo cluster (Machacek et al. 2006) produced density jumps that are similar in magnitude. Based on this and the near constant ICM temperature and high metal abundance (particularly Fe) in the stripped halo found by Hayakawa et al. (2006) and Sato et al. (2007), these edges appear to be the so-called “iron

fronts” (Markevitch & Vikhlinin 2007, Sect. 2.5), where a substantial decrease in the Fe abundance beyond the edge is observed.

Moreover, the northern part of the Flying Fox spatially overlaps with the eastern and southern shocks along the line of sight (Fig. 3). This suggests that these weak ICM shocks partially contribute to the diffuse radio emission. Although diffusive shock acceleration (e.g., Drury 1983) is inefficient at weak ICM shocks, an older population of cosmic rays that originated from past turbulence and AGN outbursts can get re-accelerated from these shocks and emit synchrotron radiation (e.g., Kang et al. 2007, 2012). Such a population could originate from the fossil radio plasma of a previous outburst from the radio-loud AGN of NGC 3311. This hypothesis is supported by the steep average spectral index of $\alpha = -1.4$ observed by Kurahara et al. (2024). However, they also reported a brightness decrease from $3.2 \text{ mJy beam}^{-1}$ in the south-east to $\approx 0.7 \text{ mJy beam}^{-1}$ in the north-west, which hints at an additional contribution to the Flying Fox from the ram-pressure stripping of NGC 3312 (e.g., Hess et al. 2022) due to its proximity to the southern tail of the radio emission. Therefore, based on our analysis, the most plausible formation scenario of Flying Fox is that the brighter south-eastern section of the source is the fossil radio emission from NGC 3311 with some contribution from NGC 3312. Furthermore, the eastern and southern weak ICM shocks re-inject energy into the fossil plasma closer to NGC 3311 and produce the weaker north-western section of the Flying Fox.

3.4. eROSITA normalization, temperature, and metallicity profiles

For the estimation of the normalization, temperature, and metallicity profiles of Abell 1060, we extracted the cluster spectrum from seven radial annuli within the radial range $0 \leq R \leq R_{200}$. The widths of these annuli are optimized such that the S/N declines by a maximum of 2σ per bin. Next, we fitted the cluster spectra with the full spectral model (Eq. 1) following the procedure described in Sect. 2.4. The best-fit parameters thus obtained for each bin are mentioned in Table E.1 and the normalization, temperature, and metallicity profiles are displayed in Fig. 13.

In Fig. 13 (top), we display the radial distribution of the apec_{ICM} normalization per unit area until R_{200} . The apec normalization is described as

$$\text{Normalization} = \frac{10^{-14}}{4\pi[D_A(1+z)]^2} \text{EM}, \quad (6)$$

where D_A is the angular diameter distance in cm and EM is the emission measure, which depends on the electron number density (n_e) as

$$\text{EM} = \int n_e^2 dV, \quad (7)$$

where dV is the volume element in cm^3 . We observe the highest normalization in the central bin, followed by a steady decline by two orders of magnitude until R_{200} in the profile. This is because the apec normalization has an n_e^2 dependence (Eqs. 6 and 7) and Abell 1060 lacks substructures (Sect. 3.1). We note that the normalization of the outermost radial bin is marginally higher (0.85σ) than that of the previous bin. Next, we present the eROSITA temperature profile of Abell 1060 in Fig. 13 (middle). We observe a peak temperature of $k_B T = 2.84^{+0.18}_{-0.19} \text{ keV}$ from the innermost bin, followed

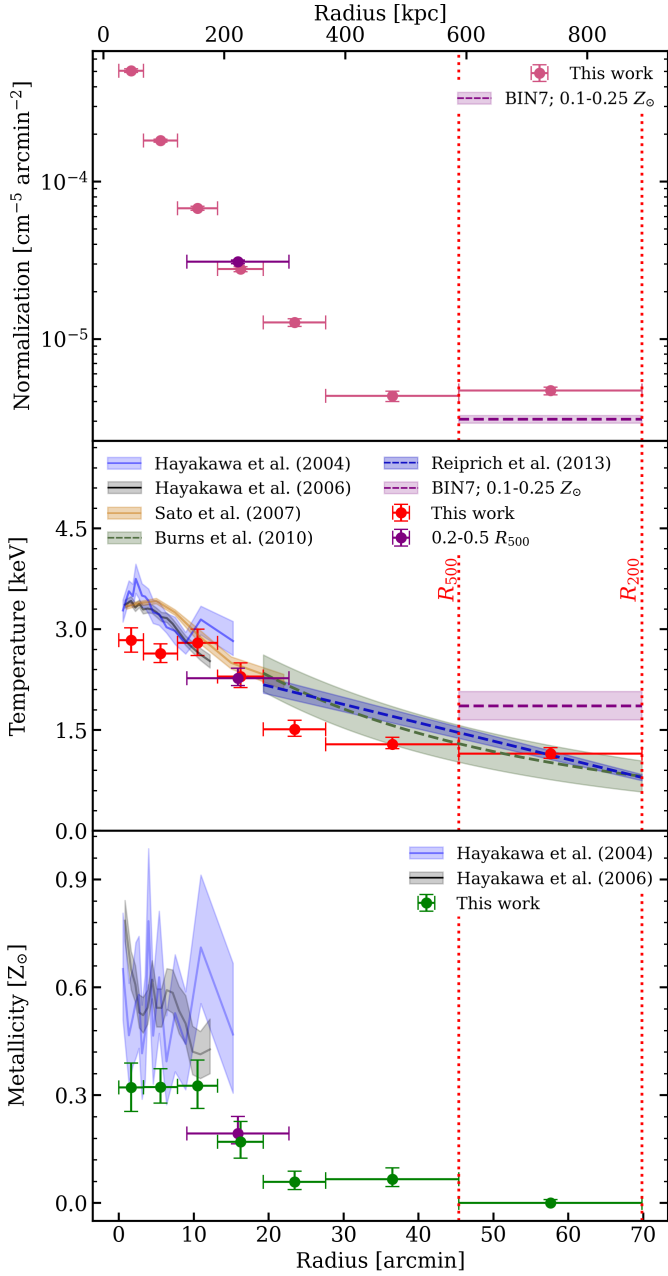


Fig. 13. eROSITA normalization (top), temperature (middle), and metallicity (bottom) profiles of Abell 1060 within the radial range $0 \leq R \leq R_{200}$. The previous estimates of the temperature and metallicity profiles and the expected profiles in the outskirts from Burns et al. (2010) and Reiprich et al. (2013) are plotted using colored solid and dashed lines, respectively. Additionally, their respective 1σ uncertainties are also plotted using colored shaded regions.

by a decline of a factor of ≈ 2.5 , with the temperature between R_{500} and R_{200} being $k_B T = 1.15^{+0.07}_{-0.09}$ keV. This absence of a central temperature drop in the ICM is characteristic of an NCC cluster. Furthermore, we obtained an average ICM temperature of $\langle k_B T \rangle = 2.27^{+0.15}_{-0.11}$ keV from the $0.2-0.5R_{500}$ annulus, whereas previous ASCA, Chandra, XMM-Newton, and Suzaku profiles (e.g., Tamura et al. 2000; Furusho et al. 2001; Hayakawa et al. 2004, 2006; Sato et al. 2007) unanimously reported an average temperature of $\langle k_B T \rangle \gtrsim 3.1$ keV. This variation in ICM temperatures is likely the combined effect of the following: 1) Chandra,

XMM-Newton, and Suzaku have a harder energy response as compared to eROSITA, and 2) the ICM has a multi-temperature structure, and the cooler, high EM component dominates the emission-weighted best-fit temperature estimate (Mazzotta et al. 2004). Within $R \approx 8'$, our profile is consistent within the cross-calibration limits between Chandra, XMM-Newton, Suzaku, and eROSITA (e.g., Kettula et al. 2013; Migkas et al. 2024), which suggests that the cooler ICM component present there is not significantly cooler. However, in the radial range $8' \leq R \leq 27'$, the previous temperature profiles are unexpectedly consistent with our profile. We additionally compared our profile in the radial range $0.28R_{200} \leq R \leq R_{200}$ ($19'29 \leq R \leq 69'82$) to the average temperature profile obtained from hydrodynamical simulations by Burns et al. (2010) and 162 Suzaku temperature measurements from Reiprich et al. (2013), both of which are normalized using the average temperature of $\langle k_B T \rangle = 2.27^{+0.15}_{-0.11}$ keV (green and blue dashed lines and shaded regions in Fig. 13 middle). We note that our profile is broadly consistent with the average profiles; however, it marginally underestimates the temperatures between $19'29 \leq R \leq 45'38$, which again suggests the presence of a cooler, high EM component.

From Fig. 13 (bottom), we note that the best-fit metallicity profile of Abell 1060 follows a similar trend as our temperature profile. We observe nearly a constant metallicity of $Z \approx 0.33 Z_\odot$ until $R = 13'2$ followed by a decline of a factor of ≈ 5.5 at R_{500} . We also estimated an average metallicity of $\langle Z \rangle = 0.19^{+0.05}_{-0.03} Z_\odot$ from the $0.2-0.5R_{500}$ annulus. Moreover, in the radial range $13'2 \leq R \leq R_{200}$, we observe a notably low average metallicity of $Z = 0.04 Z_\odot$, as the $R_{500}-R_{200}$ annulus fails to yield a non-zero estimate due to a poor S/N (Table E.1). Therefore, we investigated the effect of fixing ICM metallicity to expected values in the outskirts on the temperature estimates within the same radial range. First, we removed the $19'29 \leq R \leq 27'62$ annulus, increased the bin widths of its preceding and subsequent annuli, and fixed the metallicity to $0.15 Z_\odot$. Moreover, we reduced the model degrees of freedom (d.o.f.) by fixing the CXB normalizations to the best-fit values obtained during the CXB fitting. We observed no deviations in the best-fit temperatures as compared to our original temperature profile in Fig. 13 (middle). Next, we fixed the metallicity of the $R_{500}-R_{200}$ annulus to multiple values in the range $0.1 \leq Z \leq 0.25 Z_\odot$ and obtained higher best-fit temperatures and lower normalizations by 3.4σ and 5.2σ , respectively (purple dashed line and shaded region in Fig. 13). This is because of the degeneracy between metallicity, temperature, and normalization.

Furthermore, we compared our metallicity profile with Chandra and XMM-Newton profiles from Hayakawa et al. (2004, 2006) by applying a correction factor of 1.48, to correct for the difference in solar abundance tables (e.g., Veronica et al. 2025). This factor is the ratio of the assumed solar Fe/H values in Anders & Grevesse (1989) and Asplund et al. (2009). In Fig. 13 (bottom), both these profiles, depicted by the blue and grey shaded regions, show higher metallicities than our profiles in the two innermost annuli by 5.9σ and 2.1σ , respectively. In general, the Chandra profile fluctuates around an average metallicity of $Z = 0.59 Z_\odot$ with several values being marginally in agreement with our values. On the contrary, the XMM-Newton profile shows a more expected decline from $Z = 0.79 Z_\odot$ in the innermost bin to $Z = 0.43 Z_\odot$ at $R = 12'16$. This overall underestimation of ICM metallicity, coupled with the possible multi-temperature structure, can be explained by the so-called “Fe bias,” which is a spectral fitting artifact where a single-temperature apec model consistently yields low best-fit Fe abundances when fitted to a two/multi-temperature plasma spectrum

(e.g., Buote 2000; Gu et al. 2012; Veronica et al. 2025).

Furthermore, based on our imaging and spectral analyses, Abell 1060 showcases intermediate CC and NCC cluster properties. The flat plateau within $R = 13'2$ in our temperature and metallicity profiles, as well as the weak central surface brightness cusp, are initial signs of radiative cooling, which is indicative of a transitional state known as a WCC (Hudson et al. 2010). Moreover, the central cooling time range of the ICM within $R < 5'$ in the ACCEPT sample (Cavagnolo et al. 2009) is between 3.69 and 5.33 Gyr, which is typical of WCC clusters. This timescale is also consistent with the estimated last major merger period of ~ 3 Gyr by Sato et al. (2007). Furthermore, Hudson et al. (2010) also classified Abell 1060 as a WCC cluster based on the cooling time in their CC diagnostics of the HIFLUGCS clusters. On the other hand, Hayakawa et al. (2006) reported small-scale temperature enhancements at $R \approx 7'$ in the south-east direction that originated less than a gigayear ago. However, we do not detect any signs of that feature in our eROSITA surface brightness or temperature profiles.

4. Summary and conclusion

In this work, we performed a thorough imaging and spectral analysis using eRASS:4 data with a FoV of ≈ 300 square degrees centered on Abell 1060 that included a highly varying and complex CXB structure. Moreover, we used the archival Chandra observation of Abell 1060 to probe the ICM within $R = 4'$. We summarize our results from these analyses below:

- We determined that Abell 1060 has a relaxed ICM morphology within R_{500} from the 0.2–2.3 keV eROSITA image. The ICM is spherically symmetric and lacks any major substructures. The X-ray peak coincides with NGC 3311 along the line of sight (Sect. 3.1).
- We analyzed the NED spectroscopic redshift distribution of Abell 1060 within R_{200} and obtained a best-fit $\mu_{\text{spec}} \pm \sigma_{\text{spec}} = 0.0121 \pm 0.0027$ via a Gaussian fit. We also obtained nearly identical values from an adaptive $n\sigma$ -clipping algorithm. The redshift distribution is unimodal and the peak in the 2D galaxy distribution displays high spatial correlation with the X-ray peak (Sect. 3.2).
- We did not find a galaxy overdensity directly between Abell 1060 and the Antlia cluster in the redshift range $0 \leq z \leq 0.03$. In the redshift range $0.03 \leq z \leq 0.08$, several indirect overdensities that connect the two clusters are apparent in the NED and 2MASS maps (Fig. B.3). However, the Antlia SNR obscures any possible filamentary X-ray emission present there (Sects. 3.1 and 3.2).
- The modified β -model (Eq. 2) is a good fit ($\chi^2_{\text{red}} = 0.9$) to the 0.2–2.3 keV eROSITA surface brightness profile until $3R_{200}$ and successfully models the weak central surface brightness cusp. The best-fit β and r_c parameters are consistent with previous estimates from Hayakawa et al. (2004) and Chen et al. (2007).
- The outskirts of Abell 1060 are actively accreting baryons as we discovered multiple soft X-ray excesses with high spatial correlation with the 2D galaxy distribution beyond R_{200} . The peak significance of the northern and north-western excesses is 5.8σ and 3.6σ , respectively. The northern excess, in particular, has a high median significance of 3.4σ between R_{200} and $3R_{200}$. However, the foreground structure in region C makes it difficult to determine the true extent of the south-western excess (Sect. 3.3.1).

- We discovered three potential iron fronts at the eastern, southern, and northern edges of the ram-pressure stripped halo of NGC 3311 with $M = 1.25^{+0.09}_{-0.08}$, $1.53^{+0.23}_{-0.23}$, $0.99^{+0.07}_{-0.06}$, respectively. The eastern and southern fronts, together with NGC 3312, and the fossil radio emission from NGC 3311, likely contribute to the Flying Fox (Sect. 3.3.2).
- We estimated an average ICM temperature and metallicity of $\langle k_B T \rangle = 2.27^{+0.15}_{-0.11}$ keV and $\langle Z \rangle = 0.19^{+0.05}_{-0.03} Z_{\odot}$, respectively from the 0.2–0.5 R_{500} annulus. The temperature profile is broadly consistent with the average profiles from Burns et al. (2010) and Reiprich et al. (2013) in the radial range $0.28R_{200} \leq R \leq R_{200}$. However, the underestimation of ICM temperature and metal abundance in several radial bins is likely because of the Fe bias (Sect. 3.4).
- We classified Abell 1060 as a WCC cluster based on our observations of the flat plateau in the temperature profile within $R = 13'2$, weak surface brightness cusp, no current signs of AGN activity, relaxed morphology within R_{500} , and a central cooling time between 3.69–5.33 Gyr in the ACCEPT sample (Cavagnolo et al. 2009). This behavior is likely caused by the initiation of radiative cooling in the core following the last major merger event.

Through our employed combination of eROSITA and Chandra observations in this work, we significantly expanded the current understanding of the physical properties of Abell 1060's ICM for the first time beyond R_{500} . Furthermore, the correlation between X-ray features and multiwavelength data from TGSS, 2MASS, and NED showcased non-thermal emission, a unique dynamical state, and the surrounding large-scale structure. However, future observations of the central $R = 10'$ of the cluster using LOFAR (van Haarlem et al. 2013) and high X-ray spectral resolution of XRISM (XRISM Science Team 2020) will help us better understand the ICM kinematics and the radio emissions from NGC 3309, NGC 3311, and NGC 3312. Furthermore, observations of potential X-ray filamentary emission using HUBS (Bregman et al. 2023) along the optical/IR galaxy overdensities between Abell 1060 and the Antlia cluster will be useful to map the WHIM filaments closer to $3R_{200}$.

Acknowledgements. JD acknowledges funding by the Federal Ministry of Education and Research (BMBF) and the Ministry of Culture and Science of the State of North Rhine-Westphalia (MWK) as part of TRA Matter and the Excellence Strategy of the federal and state governments. This work is based on data from eROSITA, the soft X-ray instrument aboard SRG, a joint Russian-German science mission supported by the Russian Space Agency (Roskosmos), in the interests of the Russian Academy of Sciences represented by its Space Research Institute (IKI), and the Deutsches Zentrum für Luft- und Raumfahrt (DLR). The SRG spacecraft was built by Lavochkin Association (NPOL) and its subcontractors, and is operated by NPOL with support from the Max Planck Institute for Extraterrestrial Physics (MPE). The development and construction of the eROSITA X-ray instrument was led by MPE, with contributions from the Dr. Karl Remeis Observatory Bamberg & ECAP (FAU Erlangen-Nürnberg), the University of Hamburg Observatory, the Leibniz Institute for Astrophysics Potsdam (AIP), and the Institute for Astronomy and Astrophysics of the University of Tübingen, with the support of DLR and the Max Planck Society. The Argelander Institute for Astronomy of the University of Bonn and the Ludwig Maximilians Universität Munich also participated in the science preparation for eROSITA. The eROSITA data shown here were processed using the eSASS software system developed by the German eROSITA consortium. This research has made use of data obtained from the Chandra Data Archive provided by the Chandra X-ray Center (CXC). We thank the staff of the GMRT that made these observations possible. GMRT is run by the National Centre for Radio Astrophysics of the Tata Institute of Fundamental Research. The Second Palomar Observatory Sky Survey (POSS-II) was made by the California Institute of Technology with funds from the National Science Foundation, the National Aeronautics and Space Administration, the National Geographic Society, the Sloan Foundation, the Samuel Oschin Foundation, and the Eastman Kodak Corporation. This publication makes use of data products from the Two Micron All Sky Survey, which is a joint project of the University of Massachusetts and the Infrared Processing and Analysis Center/California Institute of Technology, funded by the National

Aeronautics and Space Administration and the National Science Foundation. This research has made use of the NASA/IPAC Extragalactic Database, which is funded by the National Aeronautics and Space Administration and operated by the California Institute of Technology.

References

- Anders, E. & Grevesse, N. 1989, *Geochim. Cosmochim. Acta*, 53, 197
- Arnaud, K. A. 1996, in *Astronomical Society of the Pacific Conference Series*, Vol. 101, *Astronomical Data Analysis Software and Systems V*, ed. G. H. Jacoby & J. Barnes, 17
- Asplund, M., Grevesse, N., Sauval, A. J., & Scott, P. 2009, *ARA&A*, 47, 481
- Bertin, E. & Arnouts, S. 1996, *A&AS*, 117, 393
- Bregman, J., Cen, R., Chen, Y., et al. 2023, *Science China Physics, Mechanics, and Astronomy*, 66, 299513
- Brunner, H., Liu, T., Lamer, G., et al. 2022, *A&A*, 661, A1
- Bulbul, E., Liu, A., Kluge, M., et al. 2024, *A&A*, 685, A106
- Buote, D. A. 2000, *MNRAS*, 311, 176
- Burns, J. O., Hallman, E. J., Gantner, B., Motl, P. M., & Norman, M. L. 2008, *ApJ*, 675, 1125
- Burns, J. O., Skillman, S. W., & O’Shea, B. W. 2010, *ApJ*, 721, 1105
- Cash, W. 1979, *ApJ*, 228, 939
- Cavagnolo, K. W., Donahue, M., Voit, G. M., & Sun, M. 2009, *ApJS*, 182, 12
- Cavaliere, A. & Fusco-Femiano, R. 1976, *A&A*, 49, 137
- Cen, R. & Ostriker, J. P. 1999, *ApJ*, 514, 1
- Chen, Y., Reiprich, T. H., Böhringer, H., Ikebe, Y., & Zhang, Y. Y. 2007, *A&A*, 466, 805
- Courtois, H. M., Pomarède, D., Tully, R. B., Hoffman, Y., & Courtois, D. 2013, *AJ*, 146, 69
- Dietl, J., Pacaud, F., Reiprich, T. H., et al. 2024, *A&A*, 691, A286
- Dong, R., Rasmussen, J., & Mulchaey, J. S. 2010, *ApJ*, 712, 883
- Drury, L. O. 1983, *Reports on Progress in Physics*, 46, 973
- Eckert, D., Finoguenov, A., Ghirardini, V., et al. 2020, *The Open Journal of Astrophysics*, 3, 12
- Einasto, M., Einasto, J., Tago, E., Müller, V., & Andernach, H. 2001, *AJ*, 122, 2222
- Foreman-Mackey, D., Hogg, D. W., Lang, D., & Goodman, J. 2013, *PASP*, 125, 306
- Freyberg, M., Perinati, E., Pacaud, F., et al. 2020, in *SPIE*, Vol. 11444, *Space Telescopes and Instrumentation 2020: Ultraviolet to Gamma Ray*, ed. J.-W. A. den Herder, S. Nikzad, & K. Nakazawa, 114441O
- Fruscione, A., McDowell, J. C., Allen, G. E., et al. 2006, in *SPIE*, Vol. 6270, *Observatory Operations: Strategies, Processes, and Systems*, ed. D. R. Silva & R. E. Doherty, 62701V
- Furusho, T., Yamasaki, N. Y., & Ohashi, T. 2002, *arXiv e-prints*, astro
- Furusho, T., Yamasaki, N. Y., Ohashi, T., et al. 2001, *PASJ*, 53, 421
- Ghirardini, V., Bulbul, E., Hoang, D. N., et al. 2021, *A&A*, 647, A4
- Gu, L., Xu, H., Gu, J., et al. 2012, *ApJ*, 749, 186
- Hayakawa, A., Furusho, T., Yamasaki, N. Y., Ishida, M., & Ohashi, T. 2004, *PASJ*, 56, 743
- Hayakawa, A., Hoshino, A., Ishida, M., et al. 2006, *PASJ*, 58, 695
- Hess, K. M., Kotulla, R., Chen, H., et al. 2022, *A&A*, 668, A184
- HI4PI Collaboration, Ben Bekhti, N., Flöer, L., et al. 2016, *A&A*, 594, A116
- Hickox, R. C. & Markevitch, M. 2006, *ApJ*, 645, 95
- Hudson, D. S., Mittal, R., Reiprich, T. H., et al. 2010, *A&A*, 513, A37
- Intema, H. T., Jagannathan, P., Mooley, K. P., & Frail, D. A. 2017, *A&A*, 598, A78
- Jarrett, T. H., Chester, T., Cutri, R., et al. 2000, *AJ*, 119, 2498
- Kang, H., Ryu, D., Cen, R., & Ostriker, J. P. 2007, *ApJ*, 669, 729
- Kang, H., Ryu, D., & Jones, T. W. 2012, *ApJ*, 756, 97
- Kettula, K., Nevalainen, J., & Miller, E. D. 2013, *A&A*, 552, A47
- Kuntz, K. D. & Snowden, S. L. 2000, *ApJ*, 543, 195
- Kurahara, K., Akahori, T., Oki, A., Omiya, Y., & Nakazawa, K. 2024, *PASJ*, 76, L8
- Kwast, T. 1966, *Acta Astron.*, 16, 45
- Landau, L. & Lifshitz, E. 1987, in *Fluid Mechanics (Second Edition)*, second edition edn., ed. L. Landau & E. Lifshitz (Pergamon), 313–360
- Lindblad, P. O., Jorsater, S., & Sandqvist, A. 1985, *A&A*, 144, 496
- Liu, A., Bulbul, E., Ghirardini, V., et al. 2022, *A&A*, 661, A2
- Liu, W., Chiao, M., Collier, M. R., et al. 2017, *ApJ*, 834, 33
- Luo, B., Brandt, W. N., Xue, Y. Q., et al. 2017, *ApJS*, 228, 2
- Machacek, M., Dosaj, A., Forman, W., et al. 2005, *ApJ*, 621, 663
- Machacek, M., Jones, C., Forman, W. R., & Nulsen, P. 2006, *ApJ*, 644, 155
- Markevitch, M. & Vikhlinin, A. 2007, *Phys. Rep.*, 443, 1
- Mazzotta, P., Rasia, E., Moscardini, L., & Tormen, G. 2004, *MNRAS*, 354, 10
- McCall, H., Reiprich, T. H., Veronica, A., et al. 2024, *A&A*, 689, A113
- McLean, B. J., Greene, G. R., Lattanzi, M. G., & Pirenne, B. 2000, in *Astronomical Society of the Pacific Conference Series*, Vol. 216, *Astronomical Data Analysis Software and Systems IX*, ed. N. Manset, C. Veillet, & D. Crabtree, 145
- Migkas, K., Kox, D., Schellenberger, G., et al. 2024, *A&A*, 688, A107
- Misgeld, I., Mieske, S., Hilker, M., et al. 2011, *A&A*, 531, A4
- Molendi, S. & Pizzolato, F. 2001, *ApJ*, 560, 194
- More, S., Diemer, B., & Kravtsov, A. V. 2015, *ApJ*, 810, 36
- Pacaud, F., Pierre, M., Refregier, A., et al. 2006, *MNRAS*, 372, 578
- Pahre, M. A. 1999, *ApJS*, 124, 127
- Piffaretti, R., Arnaud, M., Pratt, G. W., Pointecouteau, E., & Melin, J. B. 2011, *A&A*, 534, A109
- Pratt, G. W. & Arnaud, M. 2002, *A&A*, 394, 375
- Predehl, P., Andritschke, R., Arefiev, V., et al. 2021, *A&A*, 647, A1
- Predehl, P., Sunyaev, R. A., Becker, W., et al. 2020, *Nature*, 588, 227
- Ramos-Ceja, M. E., Pacaud, F., Reiprich, T. H., et al. 2019, *A&A*, 626, A48
- Reiprich, T. H., Basu, K., Ettori, S., et al. 2013, *Space Sci. Rev.*, 177, 195
- Reiprich, T. H., Sarazin, C. L., Kempner, J. C., et al. 2003, in *American Institute of Physics Conference Series*, Vol. 666, *The Emergence of Cosmic Structure*, ed. S. H. Holt & C. S. Reynolds (AIP), 319–322
- Reiprich, T. H., Veronica, A., Pacaud, F., et al. 2021, *A&A*, 647, A2
- Reiprich, T. H., Veronica, A., Pacaud, F., et al. 2025, *arXiv e-prints*, arXiv:2503.02884
- Richter, O. G. & Huchtmeier, W. K. 1983, *A&A*, 125, 187
- Richter, O. G., Materne, J., & Huchtmeier, W. K. 1982, *A&A*, 111, 193
- Sanders, J. S., Fabian, A. C., Russell, H. R., Walker, S. A., & Blundell, K. M. 2016a, *MNRAS*, 460, 1898
- Sanders, J. S., Fabian, A. C., Taylor, G. B., et al. 2016b, *MNRAS*, 457, 82
- Sarkar, A., Randall, S., Su, Y., et al. 2023, *ApJ*, 944, 132
- Sato, K., Yamasaki, N. Y., Ishida, M., et al. 2007, *PASJ*, 59, 299
- Shin, J., Woo, J.-H., & Mulchaey, J. S. 2016, *ApJS*, 227, 31
- Singh, K. P., Westergaard, N. J., & Schnopper, H. W. 1988, *ApJ*, 330, 620
- Smith, M. G. & Weedman, D. W. 1976, *ApJ*, 205, 709
- Smith, R. K., Brickhouse, N. S., Liedahl, D. A., & Raymond, J. C. 2001, *ApJ*, 556, L91
- Smyth, R. J. & Stobie, R. S. 1980, *MNRAS*, 190, 631
- Spavone, M., Iodice, E., Lohmann, F. S., et al. 2024, *A&A*, 689, A306
- Tamura, T., Day, C. S., Fukazawa, Y., et al. 1996, *PASJ*, 48, 671
- Tamura, T., Makishima, K., Fukazawa, Y., Ikebe, Y., & Xu, H. 2000, *ApJ*, 535, 602
- van Haarlem, M. P., Wise, M. W., Gunst, A. W., et al. 2013, *A&A*, 556, A2
- Veronica, A., Reiprich, T. H., Pacaud, F., et al. 2024, *A&A*, 681, A108
- Veronica, A., Reiprich, T. H., Pacaud, F., et al. 2025, *A&A*, 694, A168
- Vikhlinin, A., Burenin, R., Forman, W. R., et al. 2007, in *Heating versus Cooling in Galaxies and Clusters of Galaxies*, ed. H. Böhringer, G. W. Pratt, A. Finoguenov, & P. Schuecker, 48
- Virtanen, P., Gommers, R., Oliphant, T. E., et al. 2020, *Nature Methods*, 17, 261
- Walker, S. A., Mirakhor, M. S., Zuhone, J., et al. 2022, *ApJ*, 929, 37
- Weisskopf, M. C., Tananbaum, H. D., Van Speybroeck, L. P., & O’Dell, S. L. 2000, in *SPIE*, Vol. 4012, *X-Ray Optics, Instruments, and Missions III*, ed. J. E. Truemper & B. Aschenbach, 2–16
- Willingale, R., Starling, R. L. C., Beardmore, A. P., Tanvir, N. R., & O’Brien, P. T. 2013, *MNRAS*, 431, 394
- Wilms, J., Allen, A., & McCray, R. 2000, *ApJ*, 542, 914
- Wong, K.-W., Irwin, J. A., Wik, D. R., et al. 2016, *ApJ*, 829, 49
- XRISM Science Team. 2020, *arXiv e-prints*, arXiv:2003.04962
- Yamasaki, N. Y., Ohashi, T., & Furusho, T. 2002, *ApJ*, 578, 833
- Yeung, M. C. H., Freyberg, M. J., Ponti, G., et al. 2023, *A&A*, 676, A3
- Zheng, X., Ponti, G., Freyberg, M., et al. 2024, *A&A*, 681, A77

Appendix A: $N_{\text{H,tot}}$ map

The $N_{\text{H,tot}}$ map is prepared following the expression from Willingale et al. (2013), which is given as

$$N_{\text{H,tot}} = N_{\text{HI}} + 2N_{\text{H}_2}. \quad (\text{A.1})$$

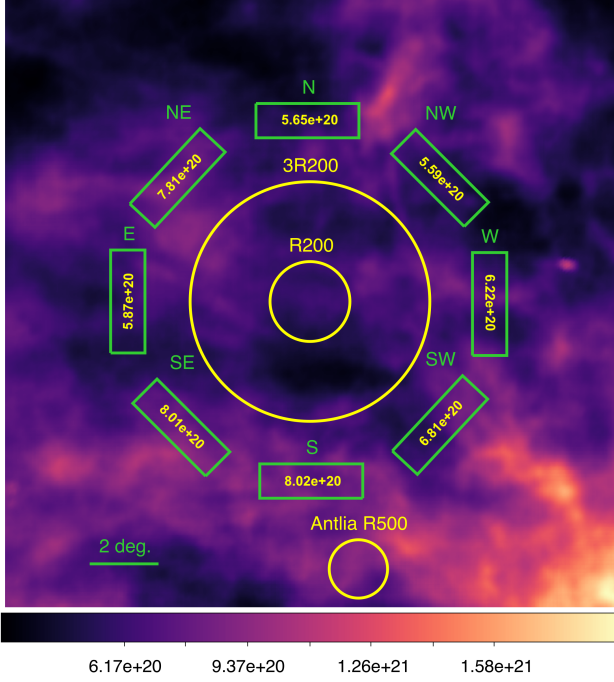


Fig. A.1. $N_{\text{H,tot}}$ map (unit is cm^{-2}) displaying the spatial variation of the total hydrogen column density in our FoV with respect to the characteristic radii of Abell 1060 and the Antlia cluster. The background boxes and their respective median $N_{\text{H,tot}}$ are annotated on the image.

Appendix B: X-ray images

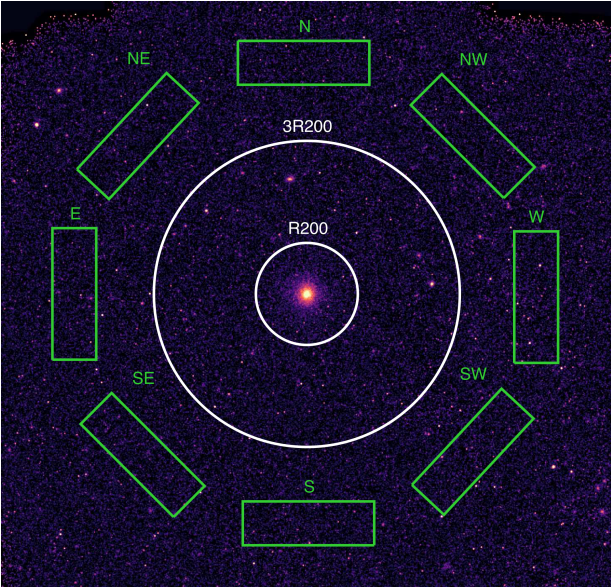


Fig. B.1. Fully corrected eROSITA image in the 0.2-2.3 keV band, smoothed using a Gaussian kernel of 18 pixels width. The eight background regions used to estimate the CXB for the surface brightness and spectral analyses are displayed using green boxes.

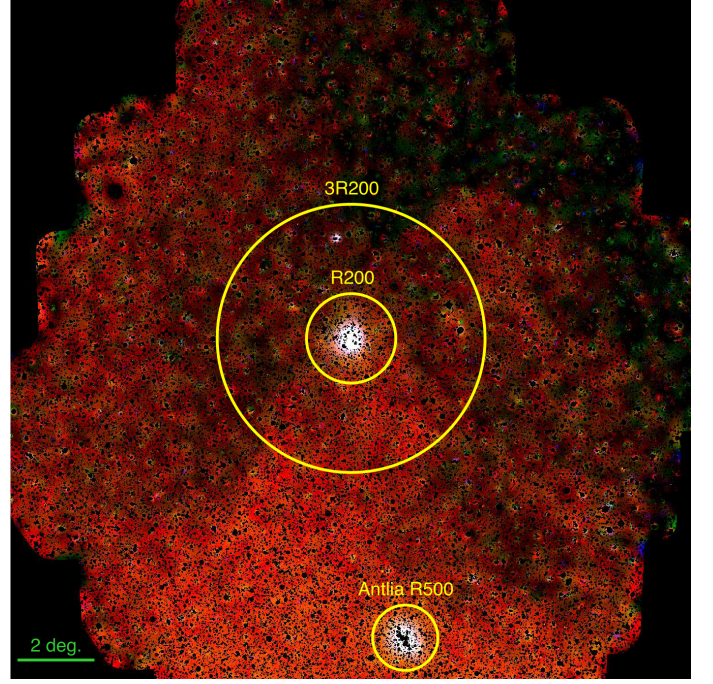


Fig. B.2. Point source removed eROSITA wavelet filtered RGB image, prepared using the energy bands 0.2-0.8 keV (red), 0.8-1.2 keV (green), and 1.2-2.3 keV (blue).

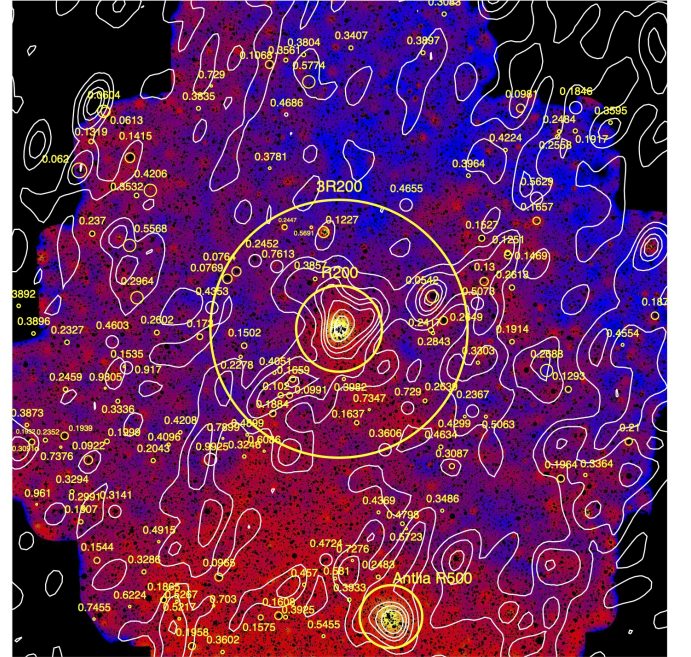


Fig. B.3. Same as Fig. 6, overlaid with 2MASS galaxy distribution contours and eRASS:1 background clusters. The clusters' positions are plotted in yellow (circle represents the R_{500}) and white (unknown R_{500} , marked via circles of $R = 10'$).

Appendix C: X-ray surface brightness analysis

We performed the surface brightness analysis of Abell 1060 using eROSITA and Chandra to study its brightness distribution and to characterize the morphology of its ICM. The eROSITA

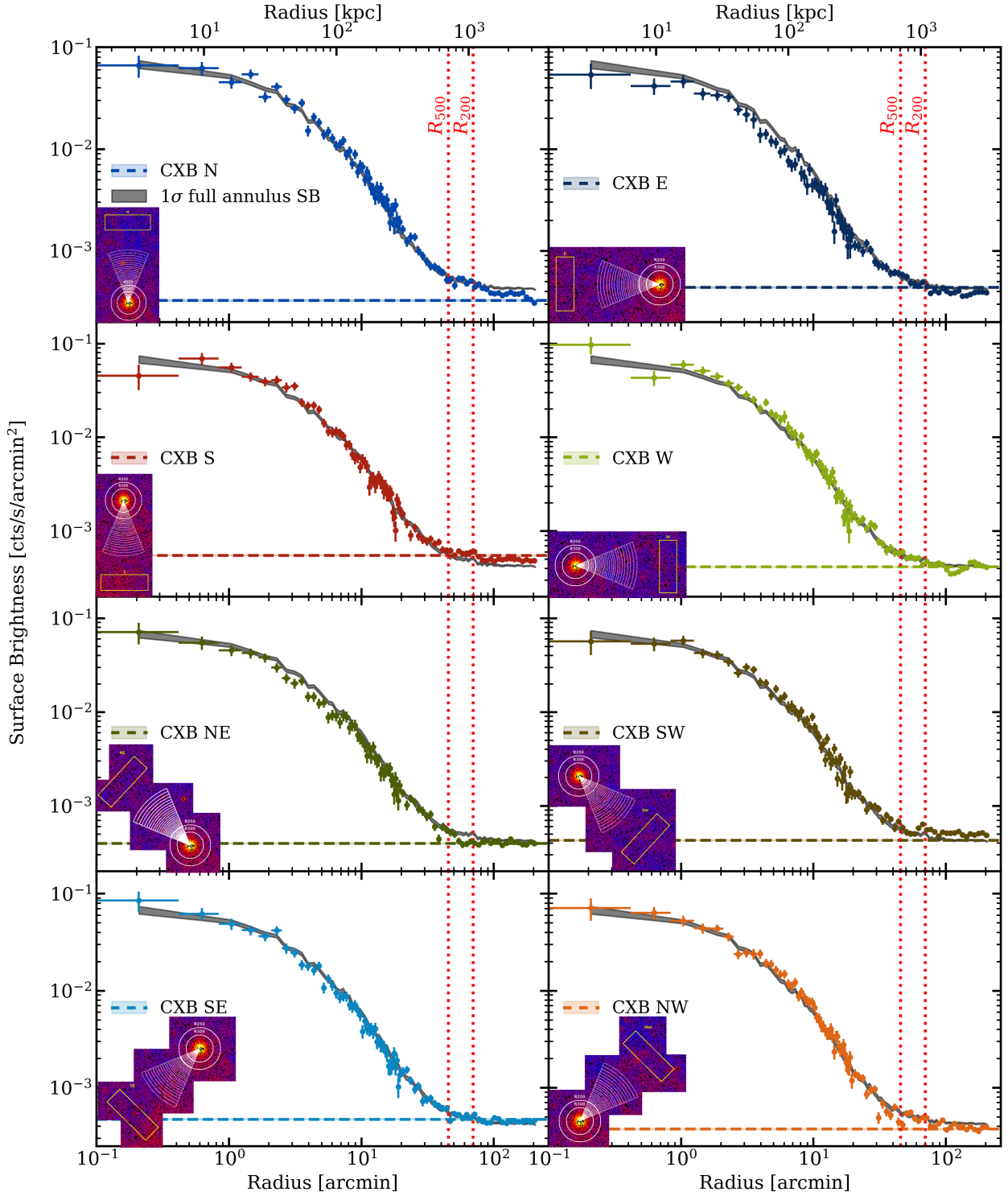


Fig. C.1. eROSITA sector surface brightness profiles in the 0.2-2.3 keV band. The gray shaded region depicts the 1σ error bars of the full annulus profile. The inset in each sector plot showcases the orientation of the sector and the background box used to estimate the CXB level.

profile is centered on the X-ray peak, R.A. = 159°184 and Dec. = -27°527, which is estimated within an aperture of $R = 2'$ centered on Abell 1060's core in the fully corrected 0.2-2.3 keV eROSITA image. We used concentric radial annuli for the profile with a constant binning of $25''$ (approximate width of the eROSITA PSF) in the radial range $0 \leq R \leq R_{2500}$, followed by logarithmic bins until $3R_{200}$. For the extraction, we used the eROSITA TM0 photon image, the $N_{H,\text{tot}}$ corrected exposure map

(single TM version), and the PIB map in the 0.2-2.3 keV band. Similarly, for Chandra, the cleaned image, the exposure map (in seconds), and the background map in the 0.5-2.3 keV are used. We used the FT00LS⁸ task `funcnts` to calculate the total counts (Σ cts), the statistical uncertainty ($\sqrt{\Sigma}$ cts), and the area within a

⁸ <https://heasarc.gsfc.nasa.gov/ftools/>

Table C.1. Best-fit parameters for Eq. 3 from each sector along with the estimated M of the surface brightness discontinuity. The goodness of a fit is described using $\chi^2/\text{d.o.f.}$.

Sector	α_1	α_2	r_f^*	$S_X(0)^\dagger$	J	$\chi^2/\text{d.o.f.}$	M
East	$-1.04^{+0.50}_{-0.66}$	$0.85^{+0.02}_{-0.02}$	$0.75^{+0.04}_{-0.04}$	$-0.95^{+0.10}_{-0.10}$	$1.36^{+0.16}_{-0.16}$	56.86/40.00	$1.25^{+0.09}_{-0.08}$
South	$-2.09^{+1.14}_{-1.91}$	$0.64^{+0.03}_{-0.03}$	$0.51^{+0.07}_{-0.10}$	$-0.84^{+0.16}_{-0.18}$	$1.76^{+0.41}_{-0.41}$	13.70/10.00	$1.53^{+0.23}_{-0.23}$
North	$0.05^{+0.20}_{-0.25}$	$0.85^{+0.02}_{-0.02}$	$0.88^{+0.01}_{-0.01}$	$-1.31^{+0.09}_{-0.09}$	$0.99^{+0.12}_{-0.11}$	51.20/31.00	$0.99^{+0.07}_{-0.06}$

* unit is arcmin.

 † units are counts $\text{s}^{-1} \text{ arcmin}^{-2}$ and values are in log base 10.

particular region. We then used the expression

$$\text{Surface Brightness} = \frac{\Sigma \text{cts}_{\text{photon}} - \Sigma \text{cts}_{\text{PIB}}}{\bar{t}_{\text{exp}} \cdot A}, \quad (\text{C.1})$$

where $\Sigma \text{cts}_{\text{photon}}$ and $\Sigma \text{cts}_{\text{PIB}}$ are the total counts within a region in the X-ray image and the PIB image, respectively, \bar{t}_{exp} is the average exposure time per pixel, i.e., the total exposure counts in the region normalized by the total number of pixels, and A is the area of the region in units of arcmin^2 . The uncertainty on a surface brightness measurement is estimated by the Gaussian propagation of the statistical uncertainties on $\Sigma \text{cts}_{\text{photon}}$ and $\Sigma \text{cts}_{\text{PIB}}$.

In the outskirts, we estimated the statistical significance (in the unit of σ) of a surface brightness value extracted from a region ($\text{SB}_{\text{region}}$) as compared to the average CXB level (SB_{CXB}) using the expression

$$\text{Significance} = \frac{\text{SB}_{\text{region}} - \text{SB}_{\text{CXB}}}{\sqrt{\sigma_{\text{SB,region}}^2 + \sigma_{\text{SB,CXB}}^2}}, \quad (\text{C.2})$$

where $\sigma_{\text{SB,region}}$ and $\sigma_{\text{SB,CXB}}$ are the uncertainties on $\text{SB}_{\text{region}}$ and SB_{CXB} , respectively (e.g., [Veronica et al. 2025](#)). Similarly, we calculated the residual (in the unit of σ) between the surface brightness profiles and their respective best-fit models (Fig. 10) for each radial bin using the expression

$$\text{Residual} = \frac{\text{SB}_{\text{bin}} - \text{Model}_{\text{bin}}}{\sqrt{\sigma_{\text{SB}}^2 + \sigma_{\text{Model}}^2}}, \quad (\text{C.3})$$

where SB_{bin} and $\text{Model}_{\text{bin}}$ are the profile and model values for a particular radial bin, respectively, and σ_{SB} and σ_{Model} are their respective uncertainties.

In Fig. C.1, we display the sector surface brightness profiles in the 0.2–2.3 keV band. Within $R = 10'$, the north-eastern, north-western, south-western, and south-eastern sectors are largely consistent with the full annulus profiles. On the other hand, the northern, eastern, southern, and western sectors show distinct variations. Specifically, the eastern sector shows lower surface brightness with a mean and maximum negative deviation of 1.8σ and 3.2σ , respectively, from the full annulus profile. On the contrary, the western sector shows primarily higher surface brightness, albeit of a smaller magnitude than the eastern sector, within the same radial range. In the north and south, the profiles fluctuate around the full annulus profile, but their decline is consistent with its overall shape. Additionally, we observe a faster decline in surface brightness of 2.9σ magnitude in the north-east between $2' \leq R \leq 8'$. In addition, we display the best-fit parameters from the surface brightness analysis of the edges of the stripped halo of NGC 3311 in Table C.1.

Appendix D: CXB spectral analysis

The CXB in the vicinity of Abell 1060 is highly complex and includes various foreground substructures and emission from the Antlia SNR (Sect. 3.1). Therefore, we performed a CXB spectral analysis of the eight background spectra (Fig. A.1) to analyze the variations in the CXB and select a suitable background region for the ICM spectral analysis. We first fitted the CXB spectra with the CXB model from [Veronica et al. \(2024\)](#), which is the same as our CXB model (Eq. 1) but does not include the *nei* component. This was done to avoid the observed degeneracy between the LHB and *nei* components during a previous spectral modeling attempt. For the fit, the temperatures of the *apec*_{LHB} and *apec*_{MWH} are fixed to 0.1 keV and 0.25 keV, respectively ([Liu et al. 2017](#); [Kuntz & Snowden 2000](#)) and the spectral index of the *powerlaw* component is fixed to $\Gamma = 1.46$ ([Luo et al. 2017](#)). Additionally, we assumed solar metallicity and set the redshifts to zero for all the CXB components. Other details on the fit are consistent with the description in Sect. 2.4. The resulting best-fit normalizations per unit area of *apec*_{LHB}, *apec*_{MWH}, and *powerlaw* are displayed in Fig. D.1. Thereafter, we used our CXB model to model the emission from the Antlia SNR. The *nei* model consists of all four *apec* parameters and an additional parameter for the ionization time scale (τ). We fixed their values to the best-fit values (Table D.1) obtained from an extended region towards the south of Abell 1060 by Knies et al. (in prep). This region includes the majority of the foreground emission from the Antlia SNR between R_{200} and $\approx 4R_{200}$ in region B. Subsequently, we fixed the CXB normalizations of the rest of the CXB components to the best-fit values obtained from our initial fit and freed the *nei* normalization to fit the CXB spectra. We report a c-stat/d.o.f. ≈ 1 for all the background boxes, and the obtained best-fit *nei* normalizations per unit area are displayed in Fig. D.1 (bottom-right).

From Fig. D.1, we observe the global trends in the CXB normalizations per unit area of all the components. The 0.1 keV LHB and 0.25 keV MWH components show minimal variations between the north-west, west, and south-west background boxes. Moreover, the northern box exhibits the lowest normalizations on average for LHB and MWH by 20.74% and 28.3%, respectively, as compared to the aforementioned boxes. On the eastern side, we see increments of 30.15% and 13.5%, respectively, in the LHB and MWH normalizations between the north-eastern and the southern box, where both the normalizations are the highest. This result is consistent with the observed prominence of the foreground emission from region B and the extended foreground bubble from region A in the 0.2–0.8 keV band, as observed in Fig. B.2. As for the harder background emission from the unresolved AGN, the highest and lowest normalizations between all the boxes vary only by a factor of 1.24. Furthermore, we note that the 0.18 keV *nei* component shows the highest EM in the south and south-east, and declines azimuthally clockwise. Overall, the combined EM of the CXB is the highest in the south

Table D.1. Spectral parameters obtained from the CXB spectral analysis of the north-western background box (labeled “NW” in Fig. A.1). The “Status” column describes whether the respective parameter was free to vary or fixed during the ICM spectral analysis using the full spectral model (Eq. 1).

Component	Parameter	Value	Status
apec _{LHB}	Norm [$\text{cm}^{-5}\text{arcmin}^{-2}$]	$2.55^{+0.10}_{-0.13} \times 10^{-6}$	Free
	$k_B T$ [keV]	0.1	Fixed
	Abundance [Z_\odot]	1	Fixed
	Redshift	0	Fixed
apec _{MWH}	Norm [$\text{cm}^{-5}\text{arcmin}^{-2}$]	$6.55^{+0.37}_{-0.28} \times 10^{-7}$	Free
	$k_B T$ [keV]	0.25	Fixed
	Abundance [Z_\odot]	1	Fixed
	Redshift	0	Fixed
nei	Norm [$\text{cm}^{-5}\text{arcmin}^{-2}$]	$5.30^{+1.33}_{-2.59} \times 10^{-8}$	Free
	$k_B T$ [keV]	0.18	Fixed
	τ [s cm^{-3}]	2.20×10^{10}	Fixed
	Abundance [Z_\odot]	1	Fixed
	Redshift	0	Fixed
powerlaw	Norm*	$4.82^{+0.36}_{-0.26} \times 10^{-7}$	Free
	Γ	1.46	Fixed
	Redshift	0	Fixed
TBabs	N_H [cm^{-2}]	5.59×10^{20}	Fixed

* units are $\text{photons keV}^{-1} \text{cm}^{-2} \text{s}^{-1} \text{arcmin}^{-2}$.

and gradually declines towards the north-west.

Therefore, we shortlisted the north-western, western, and south-western boxes to be a good representative of the local CXB within R_{200} because of the comparatively low EM from the Antlia SNR and the stable LHB and MWH EMs. Out of these, only the north-western box has a similar median $N_{H,\text{tot}}$ compared to Abell 1060’s R_{200} . We further estimated the best-fit temperatures of the LHB and MWH components in this box by freeing their temperature parameters and fixing the nei parameters to the best-fit values in Table D.1. We observed only a minor difference in the LHB component of +0.03 keV, which produced a negligible median difference of 0.5% in the temperature profile when used as the LHB temperature during the ICM analysis. Therefore, we used the default CXB parameters from Table D.1 for our ICM analysis.

Appendix E: Normalization, temperature, and metallicity profiles

In Table E.1, we display the best-fit parameters from the ICM spectral analysis.

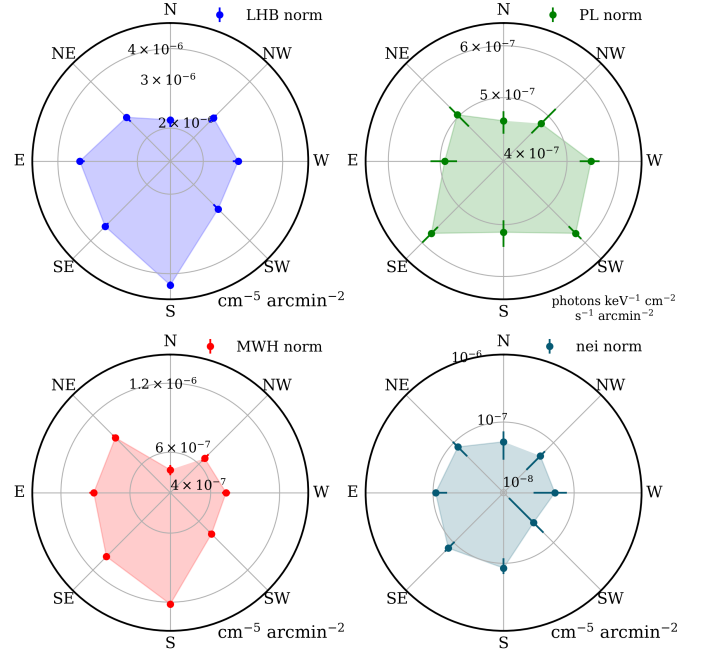


Fig. D.1. Best-fit normalizations per unit area of the apec_{LHB} (top-left), apec_{MWH} (bottom-left), nei (bottom-right), and powerlaw (top-right) components obtained by fitting the background spectra from the eight background regions shown in Fig. A.1. The units of the normalizations of each component are mentioned in the bottom right corner of all the subplots.

Table E.1. Best-fit apec_{ICM} parameters obtained from seven radial annuli in the radial range $0 \leq R \leq R_{200}$. The median $N_{\text{H,tot}}$ of each bin is listed in the second column, and the goodness of a fit is described by c-stat/d.o.f..

Radial bin [arcmin]	Median $N_{\text{H,tot}}$ [$\times 10^{20} \text{cm}^{-2}$]	Normalization [$\text{cm}^{-5} \text{arcmin}^{-2}$]	$k_{\text{B}}T$ [keV]	Metallicity [Z_{\odot}]	c-stat/d.o.f.
$0.00 \leq R \leq 3.30$	6.34	$5.05^{+0.12}_{-0.14} \times 10^{-4}$	$2.84^{+0.18}_{-0.19}$	$0.32^{+0.07}_{-0.07}$	7056.58/7331
$3.30 \leq R \leq 7.85$	6.29	$1.82^{+0.04}_{-0.04} \times 10^{-4}$	$2.64^{+0.13}_{-0.15}$	$0.32^{+0.04}_{-0.05}$	7688.27/7776
$7.85 \leq R \leq 13.20$	6.24	$6.75^{+0.20}_{-0.21} \times 10^{-5}$	$2.80^{+0.19}_{-0.20}$	$0.33^{+0.06}_{-0.07}$	7944.33/8017
$13.20 \leq R \leq 19.29$	6.13	$2.29^{+0.16}_{-0.21} \times 10^{-5}$	$2.32^{+0.52}_{-0.39}$	$0.17^{+0.05}_{-0.06}$	7849.26/ 8255
$19.29 \leq R \leq 27.62$	6.00	$1.27^{+0.01}_{-0.01} \times 10^{-5}$	$1.51^{+0.10}_{-0.14}$	$0.06^{+0.02}_{-0.03}$	8522.47/8885
$27.62 \leq R \leq R_{500}$	5.76	$4.36^{+0.34}_{-0.31} \times 10^{-6}$	$1.29^{+0.07}_{-0.10}$	$0.07^{+0.02}_{-0.03}$	10339.65/10569
$R_{500} \leq R \leq R_{200}$	5.69	$4.71^{+0.30}_{-0.23} \times 10^{-6}$	$1.15^{+0.07}_{-0.09}$	$0.00^{+0.00}_{-0.01}$	11453.33/11195
$0.2R_{500} \leq R \leq 0.5R_{500}$	6.12	$3.10^{+0.10}_{-0.06} \times 10^{-5}$	$2.27^{+0.15}_{-0.11}$	$0.19^{+0.05}_{-0.03}$	9081.10/9350